Progress in Oceanography 219 (2023) 103131

Contents lists available at ScienceDirect

Progress in Oceanography

journal homepage: www.elsevier.com/locate/pocean

Inorganic carbon and nutrient dynamics in the marginal ice zone of the Barents Sea: Seasonality and implications for ocean acidification

Elizabeth M. Jones [a,*], Melissa Chierici [a], Agneta Fransson [b], Karen M. Assmann [a], Angelika H.H. Renner [a], Helene Hodal Lødemel [a]

[a] Institute of Marine Research, Fram Centre, Tromsø, Norway
[b] Norwegian Polar Institute, Fram Centre, Tromsø, Norway

ARTICLE INFO

Keywords:
Carbonate chemistry
Nitrate
Sea-ice meltwater
Net community production
Ocean CO_2 uptake
Atlantic Water inflow
Arctic Ocean

ABSTRACT

The Barents Sea is a productive Arctic shelf sea experiencing Atlantification with ocean warming, sea ice loss and increased influence of Atlantic Water. The impact of these changes on inorganic carbon and nutrient dynamics and ocean acidification are yet to be fully understood. Seasonal variability and drivers of inorganic carbon and nutrients were determined from south of the Polar Front at 76 °N in the Barents Sea to 82 °N in the Nansen Basin, Arctic Ocean, encompassing Atlantic and Arctic regimes in summer (August 2019), winter (December 2019), winter/spring (March 2021) and spring (May 2021). Summer sea-ice meltwater was the main driver reducing total alkalinity (A_T) and dissolved inorganic carbon (C_T), corresponding to 55 % and 81 % of the total changes ΔC_T and ΔA_T, respectively, in the surface layer. Primary production reduced C_T (37 % of ΔC_T) and nutrients, particularly in ice-free waters, increasing calcium carbonate ($CaCO_3$) saturation for aragonite (Ωaragonite) from 1.3 in spring to 2.3 in summer. Net community production (NCP) in the upper 50 m was highest (1.3 mol C m^{-2}) in the Atlantic Water regimes and lowest (0.4 mol C m^{-2}) in the ice-covered Nansen Basin in summer. Mixing, organic matter remineralisation and CO_2 uptake enriched A_T, C_T and nutrients to pre-condition the water column from winter to early spring. Formation and dissolution of $CaCO_3$ from shells and ikaite in sea ice (5–13 % of ΔA_T) represented a minor A_T source from winter to spring. Highest NCP by spring (0.3 mol C m^{-2}) occurred in a transient Atlantic-like regime over the shelf slope. Atmospheric CO_2 uptake contributed up to 37 % of ΔC_T and the region was an annual CO_2 sink. Sea-ice processes and deep winter convection lowered A_T and Ωaragonite (1.12–1.14) to enhance the risk of acidification over the shelf. Future Atlantification may increase biological production, reduce meltwater dilution effects and counteract acidification in the Barents Sea. The observations reveal the importance of seasonal and spatial studies to capture variability in inorganic carbon and nutrient cycling, driven by numerous processes coupled to the ice-ocean system that may exacerbate or alleviate ocean acidification in Arctic shelf seas.

1. Introduction

The Arctic Ocean and the seasonally ice-covered shelf seas are particularly vulnerable to ocean acidification as the solubility of carbon dioxide (CO_2) increases in cold water and fresher polar waters have lower total alkalinity (A_T), which is the natural buffer against acidity (Zeebe and Wolf-Gladrow, 2001). Ocean acidification refers to the decrease in carbonate ions in seawater that lowers the degree of saturation (Ω) of calcium carbonate ($CaCO_3$) minerals (Orr et al., 2005; Doney et al., 2009). If Ω becomes less than 1 this is an indication of vulnerability of the $CaCO_3$ shells to dissolution (Orr et al., 2005; Doney et al., 2009). Ocean acidification in the Arctic is driven by uptake of atmospheric CO_2 that increases the oceanic dissolved inorganic carbon (C_T) and freshwater inputs from melting sea ice, glacial meltwater, precipitation and river runoff (Chierici and Fransson, 2009; Fransson et al., 2013). The freshwater-driven dilution in A_T and subsequent reduction in surface water Ω occurs possibly faster than reductions in Ω due to anthropogenic CO_2 uptake (Chierici and Fransson, 2009; Yamamoto-Kawai et al., 2009; Zhang et al., 2020).

Variability of oceanic C_T and A_T is driven by seasonal physical, biogeochemical and biological processes that influence the state of ocean acidification (indicated by changing Ω). Changes in salinity from

* Corresponding author.
E-mail address: elizabeth.jones@hi.no (E.M. Jones).

https://doi.org/10.1016/j.pocean.2023.103131

Available online 28 September 2023

freshwater inputs, advection and mixing of different water masses reduce C_T and A_T through dilution and increase C_T and A_T through concentration (Friis et al., 2003), with competing effects on Ω (Chierici and Fransson, 2009; Yamamoto-Kawai et al., 2009; Zhang et al., 2020; Jones et al., 2021). Primary production and biological uptake of C_T is accompanied by small increases in A_T, which increase Ω, as concomitant uptake of nitrate with H^+ conserves electroneutrality (Brewer and Goldman, 1976; Zeebe and Wolf-Gladrow, 2001). Oppositely, organic matter respiration/remineralisation increases C_T and slightly decreases A_T, with the effect of lowering Ω. Wind-induced mixing with subsurface high-CO_2 waters can lead to reductions in surface water Ω in the absence of biological CO_2 uptake (Chierici et al., 2011; Fransson et al., 2017; Jones et al., 2021). Air-sea CO_2 fluxes influence oceanic C_T only. The seasonal retreat of the sea ice exposes surface waters to the atmosphere and enhances air-sea CO_2 fluxes, which can increase Ω through CO_2 release or decrease Ω through CO_2 uptake (Fransson et al., 2013). Dissolution of $CaCO_3$ produces two bicarbonate ions and consumes CO_2, thereby increasing A_T by a factor of two relative to the increase in C_T (Zeebe and Wolf-Gladrow, 2001). Formation of $CaCO_3$ affects A_T and C_T in the opposite direction by the same 2:1 ratio. In addition to biotic $CaCO_3$ calcite and aragonite, abiotic $CaCO_3$ ikaite ($CaCO_3{\cdot}6H_2O$) can be found in sea ice under specific thermo-haline conditions (Dieckmann et al., 2010). During sea ice formation, ikaite precipitation can occur in the brine and the minerals can be trapped within the sea ice as the brine is rejected to the underlying seawater. This process partitions A_T (as $CaCO_3$) in the ice and C_T (as dissolved CO_2 from the ikaite precipitation reaction) in the brine. During sea ice melt, ikaite is released and dissolves in the meltwater to provide a minor source of A_T and increasing Ω in surface waters influenced by seasonal sea-ice melt (Rysgaard et al., 2007; Fransson et al., 2013; 2017).

The Barents Sea is an Atlantic Water inflow shelf to the Arctic Ocean, where the advection of Atlantic-sourced waters supplies the region with heat, salt, C_T and nutrients (Reigstad et al., 2002; Carmack et al., 2006; Chierici et al., 2019). Atlantic Water also has a high A_T content and has been reported to act as a buffer to acidification through entrainment into the surface layer (Chierici et al., 2011; Jones et al., 2021). The southern part of the Barents Sea is characterised by Atlantic regimes due to inflowing Atlantic Water and is seasonally ice free (Loeng, 1991; Reigstad et al., 2002) where the Polar Front marks the transition between Atlantic and Arctic regimes (Oziel et al., 2016). The northern part of the Barents Sea is influenced by the Atlantic Water inflow in the West Spitsbergen Current along the northern shelf and the cold and low-saline Polar Water and locally formed and advected sea ice from the Arctic Ocean (Smedsrud et al., 2013; Renner et al., 2018; Lundesgaard et al., 2022). Arctic waters consist of remnants of winter cooling, convection and brine from sea ice that form a halocline separating a lower salinity surface layer affected by sea-ice melt from subsurface Atlantic Water (Onarheim et al., 2014; Lundesgaard et al., 2022). Sea-ice and ice-ocean processes contribute to dense Barents Sea water formation and provide a mechanism of CO_2 transport across the shelf and outflow into the Arctic Ocean (Skagseth et al., 2020; Rogge et al., 2023). This Barents Sea is an important region for mixing and cooling of the Atlantic Water, which influences the local sea ice cover and the extent of the marginal ice zone (MIZ).

Phytoplankton blooms are seasonal features in the MIZ of the Barents Sea, closely coupled to light availability, sea-ice extent and supply of inorganic nutrients (Reigstad et al., 2002; Tremblay et al., 2015; Assmy et al., 2017). The spring blooms result in strong uptake and seasonal cycling of inorganic nutrients and C_T through production of organic matter that drives atmospheric CO_2 uptake in surface waters over the Barents Sea shelf (Fransson et al., 2001; Carmack et al., 2006; Henley et al., 2020). Further blooms in summer and autumn can contribute significantly to primary production and carbon cycling if nutrients are resupplied through upwelling, mixing with subsurface waters and remineralisation of organic matter in the presence of sufficient light (Reigstad et al., 2002; Oziel et al., 2016). Nutrient supply from Atlantic-sourced waters to the surface layer mainly occurs in autumn and winter through vertical mixing, upwelling and tidal forcing, and in spring and summer through episodic wind-induced mixing (Randelhoff et al., 2015; Oziel et al., 2016; Randelhoff et al., 2018; Renner et al., 2018).

The Barents Sea is experiencing a rapid shift in oceanic regime due to amplification of anthropogenic climate change through warming, loss of sea ice and increased influence of Atlantic Water (Onarheim et al., 2014; Polyakov et al., 2017). The inflowing Atlantic Water has warmed in recent decades (Beszczynska-Möller et al., 2012; Skagseth et al., 2020; Smedsrud et al., 2022) and resulted in Atlantification along the inflow pathways with a shift to more Atlantic-like regimes (Årthun et al., 2012; Onarheim et al., 2014; Polyakov et al., 2017; Lind et al., 2018). Atlantification has led to expansions of temperate species northwards and changes in the ecosystem (Oziel et al., 2016; Neukermans et al., 2018; Ingvaldsen et al. 2021) and increased Atlantic Water influence has been shown to drive acidification in subsurface and intermediate waters of the Arctic Ocean (Ericson et al., 2014; Ulfsbo et al., 2018). The lowering of Ω for biotic $CaCO_3$ minerals calcite (Ωcalcite) and aragonite (Ωaragonite) through ocean acidification has important consequences for marine calcifiers (Orr et al., 2005). Calcifying phytoplankton, such as the coccolithophore Emiliania huxleyi, and zooplankton, such as the pteropod *Limacina helicina*, are key producers of calcite and aragonite, respectively, and play important roles in biogeochemical cycling and carbon fluxes in the Barents Sea (Hegseth and Sundfjord, 2008; Zamelczyk et al. 2021). Enhanced supply of nutrients with reduced sea-ice cover may increase primary production and biological carbon uptake (Randelhoff et al., 2018; Arrigo and van Dijken, 2015; Tremblay et al., 2015; Chierici et al., 2019) coupled to inputs of A_T that buffer against acidification (Jones et al., 2021). However, increased sea-ice melt increases stratification and reduces mixing, which may impede nutrient resupply from subsurface waters and limit primary production and C_T uptake (Slagstad et al., 2015; Fransson et al., 2017; Chierici et al., 2019). A shift in phytoplankton species such as from diatom- to *Phaeocystis* dominated blooms under changing sea-ice conditions is predicted to reduce carbon uptake and have impacts on the Arctic food web (Carmack et al., 2006; Wassmann et al., 2006). Furthermore, reduced A_T through meltwater dilution and limited mixing will suppress the biologically- and biogeochemically-driven enhancement of Ω (Chierici and Fransson, 2009; Yamamoto-Kawai et al., 2009; Chierici et al., 2011; Zhang et al., 2020; Jones et al., 2021).

Climate-driven changes in sea ice cover, ice-ocean processes and Atlantification have implications for biogeochemical cycling through a balance of processes that influence nutrients, C_T and A_T, which may act synergistically to enhance or alleviate the risk of ocean acidification in the Barents Sea and Arctic Ocean. However, there is currently limited understanding of the seasonal variability of inorganic carbon and nutrient cycling in the Barents Sea, particularly between Atlantic and Arctic regimes, which is essential to better understand the current and future ocean acidification state in a region experiencing environmental change. The aim of this study is to determine the seasonal dynamics and drivers of inorganic carbon and nutrient cycling and ascertain the implications for ocean acidification in the Barents Sea. This study presents carbonate chemistry and inorganic nutrient data in the full water column from summer (August 2019), winter (December 2019), winter/spring (2021) and spring (2021) across the Barents Sea shelf and slope and into the deep Nansen Basin of the Arctic Ocean. The changes in the upper ocean are linked to seasonal sea-ice cover, ice meltwater inputs, advection and mixing of different water masses, primary production/respiration, calcium carbonate processes and air-sea CO_2 exchange, across Atlantic and Arctic regimes. The results are discussed within context of the state of ocean acidification during the transitions from polar summer to winter and winter to spring in a region of the Barents Sea and Arctic Ocean already experiencing amplification of anthropogenic climate change.

2. Methods

2.1. The Barents sea seasonal sampling

Seasonal sampling was carried out in the northwestern Barents Sea along a latitudinal transect 28.8–34 °E, ~76–82 °N extending from south of the Polar Front, across the shelf and to the Nansen Basin of the Arctic Ocean (Fig. 1). Fieldwork campaigns were conducted onboard RV *Kronprins Haakon* within the framework of the Nansen Legacy project where a series of 25 hydrographic stations that included 7 process (P) stations were occupied (Table 1). The transect encompassed a natural environmental gradient that covered Atlantic and Arctic regimes of the Barents Sea shelf and slope and deep Nansen basin, and the marginal ice zone, which is defined here as the area having a monthly average minimum of 15 % sea ice concentration. Details on sampling procedures can be found in Nansen Legacy (2022).

The surveys were carried out to capture seasonal (quarterly, Q) conditions in the Barents Sea; late summer 8–23 August 2019 (Q3), winter 3–13 December 2019 (Q4), winter/spring 4–17 March 2021 (Q1), spring 30 April – 13 May 2021 (Q2). Due to the COVID-19 pandemic, the planned successive completion of the seasonal cruises was not possible and therefore Q1 and Q2 were postponed from 2020 to 2021. This introduces additional interannual variability within the seasonal signals, which will be discussed in section 3.7. Therefore, data will be discussed in terms of key patterns during each season and the changes taking place between the consecutive seasonal transitions, i.e. summer to winter 2019 and winter to spring 2021.

2.2. Sea-ice conditions

Daily sea ice concentration data derived from AMSR-2 was downloaded from the Institute of Environmental Physics, University of Bremen, Germany (Spreen et al., 2008), available at https://seaice.uni-bremen.de/sea-ice-concentration-amsr-eamsr2/.

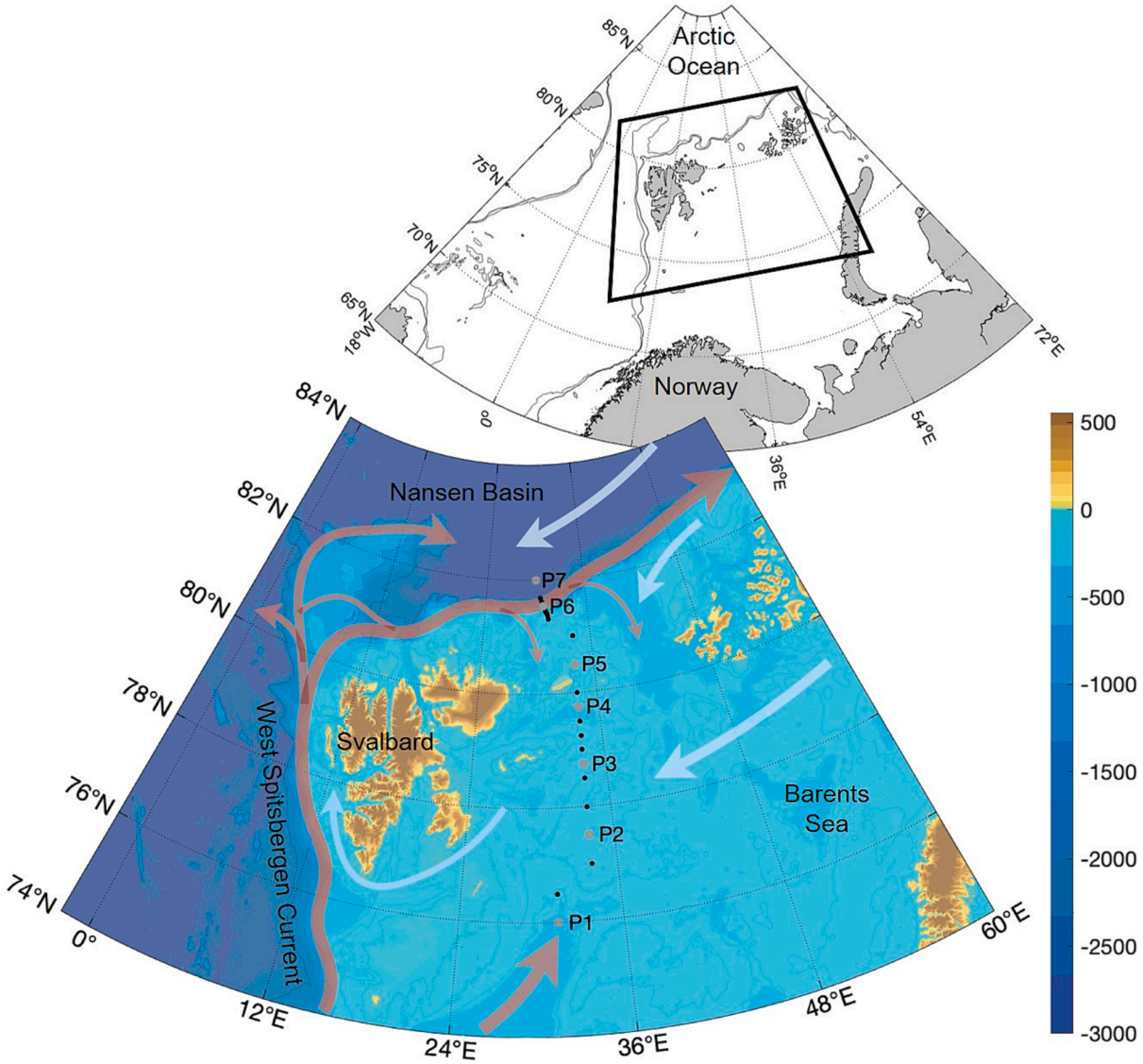

Fig. 1. Maps of Atlantic Arctic Ocean region the Barents Sea showing main regional circulation and topographic features. Red arrows depict the Atlantic Water inflow in the West Spitsbergen Current in eastern Fram Strait and the Atlantic Water pathways along the northern Svalbard shelf. Blue arrows depict the general southward flow of Arctic waters and imported sea ice, and the westward flowing Coastal Current around Svalbard. Location of the hydrographic stations are marked (black dots) and the main process (P) stations are labelled (grey dots) along the transect in the Barents Sea. Colour scale is depth (m) with isobars marked at 500, 1000, 1500, 2000, 2500 and 3000 m from bathymetric data retrieved from the International Bathymetric Chart of the Arctic Ocean IBCAO v3 (Jakobsson et al., 2012). Matlab toolbox m_map was used. (For interpretation of the references to colour in this figure legend, the reader is referred to the web version of this article.)

Table 1
Main hydrographic process (P) stations and sampling dates during summer (August 2019; Q3), winter (December 2019; Q4), winter/spring (March 2021; Q1) and spring (April-May 2021; Q2).

Station	Location	Latitude	Longitude	Bottom depth	Season/ date			
		(°N)	(°E)	(m)	summer	winter	winter/spring	spring
P1	South of Polar Front	76.00	31.22	325	08–08	12–12	05–03	30–04
P2	Shelf	77.50	33.99	190	12–08	10–12	07–03	02–05
P3	Shelf	78.75	34.00	305	13–08	9–12	08–03	03–05
P4	Shelf	79.69	34.23	332	14–08	8–12	11–03	05–05
P5	Shelf	80.50	33.99	158	16–08	6–12	12–03	07–05
P6	Slope	81.59	31.52	840	18–08	5–12	16–03	10–05
P7	Nansen Basin	81.93	29.14	3120	21–08	2–12	17–03	13–05

2.3. Hydrography and water masses

Water column hydrographic measurements were obtained using a conductivity-temperature-depth (CTD) sensor system (Sea-Bird SBE 911 +) mounted onto a General Oceanics rosette equipped with 24 10 L Niskin bottles. Seawater was typically collected at 12 depths (e.g., 10, 20, 30, 50, 100, 150, 200, then every 100 m to about 10 m above the seafloor) covering the full water column at each hydrographic station (Table 1). The CTD system was deployed through the moonpool of the vessel during Q4, Q1 and Q2 and thus the upper 10 m could not be sampled due to interference by the ship. Therefore, the upper 15 m was selected as the surface reference depth to ensure consistency between the seasons. The CTD data are reported in Gerland (2022), Ludvigsen (2022), Reigstad (2022), Søreide (2022).

Water masses in the Barents Sea and Nansen Basin (Table 2) were classified based on the definitions given in Sundfjord et al. (2020). Atlantic Water is the relatively warm and saline water mass and defined by conservative temperature (T_C) > 2 °C and absolute salinity (S_A) ≥ 35.06 g kg^{-1}. Modified Atlantic Water is a cooler variety of Atlantic Water. Polar Water is the cold and low saline surface and halocline layer. Warm Polar Water is formed by solar heating of Polar Water and mixing with Atlantic-derived waters. Intermediate Water is typically found deeper than the Atlantic-influenced water masses with lower salinity. Cold Barents Sea Dense Water (CBSDW) is defined here as $T_C \leq -1.1$ °C and is found only in the Barents Sea. Both Intermediate Water and CBDSW indicate the presence of strong winter convection due to cooling and brine release during sea-ice formation. North of the Barents Sea continental slope, Eurasian Basin Deep Water (EBDW) has an overlapping definition with Intermediate Water but includes waters deeper than 500 m north of the continental slope.

2.4. Carbonate chemistry

Seawater samples for carbonate chemistry analyses (C_T, A_T and pH_T) were drawn from the Niskin bottles into 250 mL borosilicate glass bottles. During summer 2019 (Q3), winter/spring 2021 (Q1) and spring 2021 (Q2), C_T and A_T samples were preserved with 50 µL of saturated mercuric chloride solution and stored at ~ 4 °C for post-cruise analysis at the Institute of Marine Research, Tromsø, following Dickson et al. (2007). During winter 2019 (Q4), C_T and pH samples were analysed

Table 2
Seasonal water mass, inorganic nutrients and carbonate system characteristics using bounds of conservative temperature (T_C, °C), absolute salinity (S_A; g kg^{-1}) and potential density (σ_θ, kg m^{-3}) from Sundfjord et al. (2020). Average and standard deviation (in parentheses) are shown for nitrate (NO_3, µmol kg^{-1}); phosphate (PO_4, µmol kg^{-1}); silicic acid ($Si(OH)_4$, µmol kg^{-1}); dissolved inorganic carbon (C_T, µmol kg^{-1}); total alkalinity (A_T, µmol kg^{-1}); the A_T:C_T ratio (in situ values of A_T relative to C_T); aragonite saturation state (Ωaragonite) in summer (2019, Q3), winter (2019, Q4), winter/spring (2021, Q1) and spring (2021, Q2). No CBSDW was identified in winter/spring and spring 2021 (−).

Water mass	Season (year, cruise)	NO_3 µ mol kg^{-1}	PO_4 µ mol kg^{-1}	$Si(OH)_4$ µ mol kg^{-1}	A_T µ mol kg^{-1}	C_T µ mol kg^{-1}	A_T:C_T	Ω aragonite
Warm Polar Water	Summer	4.61 (5.17)	0.37 (0.31)	2.29 (2.10)	2276 (27)	2110 (44)	1.08 (0.01)	1.76 (0.26)
(wPW)	Winter	8.84 (1.54)	0.64 (0.10)	4.25 (1.12)	2291 (12)	2151 (17)	1.07 (0.01)	1.57 (0.10)
$T_C > 0.0$ °C	Winter/spring	10.67 (0.71)	0.74 (0.06)	5.32 (0.86)	2302 (7)	2173 (12)	1.06 (0.01)	1.44 (0.11)
$S_A < 35.06$ g kg^{-1}	Spring	10.56 (1.09)	0.72 (0.07)	5.44 (1.05)	2296 (6)	2167 (10)	1.06 (0.00)	1.43 (0.09)
Polar Water	Summer	6.35 (3.46)	0.52 (0.29)	3.04 (1.33)	2259 (39)	2113 (68)	1.07 (0.02)	1.57 (0.28)
(PW)	Winter	5.79 (2.19)	0.48 (0.13)	2.85 (1.26)	2266 (26)	2135 (44)	1.06 (0.01)	1.49 (0.15)
$T_C \leq 0.0$ °C	Winter/spring	8.38 (0.88)	0.62 (0.05)	3.89 (0.70)	2282 (6)	2162 (9)	1.06 (0.00)	1.38 (0.06)
$\sigma_\theta \leq 27.97$ kg m^{-3}	Spring	7.98 (1.25)	0.59 (0.07)	4.13 (0.63)	2281 (8)	2159 (14)	1.06 (0.00)	1.39 (0.08)
Atlantic Water	Summer	11.08 (2.43)	0.74 (0.08)	4.87 (1.11)	2303 (4)	2160 (8)	1.07 (0.01)	1.54 (0.11)
(AW)	Winter	9.37 (1.57)	0.65 (0.13)	4.39 (0.82)	2304 (3)	2161 (3)	1.07 (0.00)	1.63 (0.05)
$T_C > 2$ °C	Winter/spring	11.65 (0.12)	0.78 (0.01)	5.75 (0.00)	2308 (4)	2171 (0)	1.06 (0.00)	1.40 (0.03)
$S_A \geq 35.06$ g kg^{-1}	Spring	9.80 (0.86)	0.69 (0.04)	5.00 (0.18)	2311 (1)	2164 (2)	1.07 (0.00)	1.64 (0.01)
Modified Atlantic Water	Summer	11.63 (0.66)	0.79 (0.02)	5.23 (0.89)	2303 (5)	2176 (13)	1.06 (0.01)	1.34 (0.07)
(mAW)	Winter	11.58 (0.26)	0.83 (0.04)	6.67 (1.06)	2303 (5)	2176 (13)	1.06 (0.01)	1.34 (0.06)
0.0 °C < $T_C \leq 2.0$ °C	Winter/spring	11.55 (1.01)	0.81 (0.04)	5.76 (1.33)	2307 (3)	2179 (7)	1.06 (0.00)	1.40 (0.10)
$S_A \geq 35.06$ g kg^{-1}	Spring	10.79 (1.27)	0.73 (0.08)	5.78 (1.00)	2307 (4)	2171 (5)	1.06 (0.00)	1.47 (0.12)
Intermediate Water	Summer	10.39 (0.58)	0.75 (0.04)	5.56 (0.79)	2297 (2)	2197 (6)	1.05 (0.00)	1.18 (0.05)
(IW)	Winter	10.93 (0.00)	0.84 (0.00)	7.45 (0.00)	2303 (0)	2215 (0)	1.04 (0.00)	1.13 (0.00)
−1.1 °C < $T_C \leq 0.0$ °C	Winter/spring	13.42 (0.00)	0.89 (0.00)	9.14 (0.16)	2306 (2)	2180 (6)	1.06 (0.00)	1.16 (0.02)
$\sigma_\theta > 27.97$ kg m^{-3}	Spring	13.32 (0.08)	0.89 (0.00)	8.81 (0.08)	2299 (4)	2169 (3)	1.06 (0.00)	1.18 (0.05)
Cold Barents Sea Dense	Summer	8.55 (0.48)	0.65 (0.04)	5.53 (0.88)	2300 (3)	2189 (10)	1.05 (0.00)	1.23 (0.07)
Water (CBSDW)	Winter	8.83 (0.41)	0.69 (0.00)	6.30 (0.12)	2298 (4)	2196 (6)	1.05 (0.00)	1.24 (0.02)
$T_C \leq -1.1$ °C	Winter/spring	-	-	-	-	-	-	-
$\sigma_\theta > 27.97$ kg m^{-3}	Spring	-	-	-	-	-	-	-
Eurasian Basin Deep Water (EBDW)	Summer	14.32 (0.59)	0.95 (0.04)	10.62 (1.45)	2298 (3)	2165 (10)	1.06 (0.01)	0.99 (0.14)
Depth > 500 m	Winter	13.15 (0.40)	0.93 (0.03)	10.76 (1.24)	2303 (3)	2164 (5)	1.06 (0.00)	1.06 (0.15)
−1.1 °C < $T_C \leq 0.0$ °C	Winter/spring	14.44 (0.13)	0.96 (0.01)	11.78 (0.49)	2308 (4)	2169 (6)	1.06 (0.00)	1.00 (0.11)
$S_A > 35.06$ g kg^{-1}	Spring	14.34 (0.25)	0.96 (0.02)	11.22 (0.47)	2302 (3)	2163 (4)	1.06 (0.00)	0.99 (0.12)

onboard at ~ 25 °C within approximately 24 h and A_T values were calculated using the C_T and pH measurements in the CO2SYS model.

Determination of C_T was carried out by gas extraction of acidified (10 % H_3PO_4) samples followed by coulometric titration and photometric detection (Johnson et al., 1987) using a Versatile Instrument for the Determination of Titration carbonate (VINDTA 3D, Marianda, Germany). The A_T was determined by potentiometric titration with 0.1 M hydrochloric acid in a semi-open cell using a Versatile Instrument for the Determination of Titration Alkalinity (VINDTA 3S, Marianda, Germany). Measurements of C_T and A_T were corrected against Certified Reference Materials (CRM, provided by A. G. Dickson, Scripps Institution of Oceanography, USA). The measurements precision, as determined from the average standard deviation of replicate analyses, was within ± 2 μmol kg^{-1}. Measurements for pH on the total hydrogen ion scale (pH_T) were carried out during the winter 2019 (Q4) cruise using spectrophotometric determination (Agilent 8453 Diode-array) according to Clayton and Byrne (1993) and the purified indicator dye, *meta*-cresol purple (2 mM). 3 mL of the sample was mixed with 35 μL of the indicator. The pH_T of the indicator was measured during each day using a 0.2 mm quartz cuvette. Correction for the perturbation of the indicator pH_T was performed according to Chierici et al. (1999). The precision for pH_T was determined from the average standard deviation for triplicate analyses as ± 0.001 units. The pH_T data were used in combination with the C_T data to calculate the winter 2019 A_T values using the chemical speciation model CO2SYS, as detailed in section 2.8.

2.5. Inorganic nutrients

Seawater samples for the determination of the concentration of inorganic macronutrients nitrate (NO_3), phosphate (PO_4) and silicic acid ($Si(OH_4)$) were drawn from the Niskin bottles into 20 mL pre-rinsed HDPE vials, preserved with 250 μL chloroform and stored at 4 °C. Post-cruise analysis was performed using a spectrophotometric method following standard procedures (Grasshoff et al., 2009) at the Institute of Marine Research, Bergen, Norway (Gundersen, et al., 2022). The analyser was validated by routine measurements of reference seawater from Ocean Scientific International Ltd., UK. The detection limits were 0.5 μmol kg^{-1} for NO_3, 0.06 μmol kg^{-1} for PO_4 and 0.7 μmol kg^{-1} for Si $(OH)_4$. The data are reported in (Chierici et al., 2021a; Chierici et al., 2021b; Jones et al., 2022a; Jones et al., 2022b).

2.6. Seasonal drivers of C_T and A_T in the upper ocean

Changes in the carbonate system (C_T and A_T) for each season were estimated by integrating the difference between the surface (upper 15 m) concentrations and concentrations at 120 m depth, which was below the seasonal mixed layer (Fig. S1-S2). The total change in C_T (ΔC_T) and A_T (ΔA_T) can be partitioned into the main physical, biological and biogeochemical drivers (e.g. Chierici et al., 2011; Fransson et al., 2013; Fransson et al., 2017; Jones et al., 2021) shown in Equations (1) and (2): salinity changes ($\Delta C_{T\ sal}$, $\Delta A_{T\ sal}$) from freshwater inputs, advection and mixing of different water masses, biological production of organic matter and remineralisation/respiration ($\Delta C_{T\ bio}$, $\Delta A_{T\ bio}$) and the formation and dissolution of biotic (aragonite, calcite) and abiotic (ikaite) calcium carbonate ($\Delta C_{T\ CaCO3}$, $\Delta A_{T\ CaCO3}$).

$$\Delta C_{T(surface-120m)} = \Delta C_{T\ sal} + \Delta C_{T\ bio} + \Delta C_{T\ CaCO3} + \Delta C_{T\ flux+res} \quad (1)$$

$$\Delta A_{T\ (surface-120m)} = \Delta A_{T\ sal} + \Delta A_{T\ bio} + \Delta A_{T\ CaCO3} \quad (2)$$

Changes in C_T and A_T due to salinity changes were estimated by firstly carrying out salinity normalisation of C_T and A_T ($C_{T\ sal}$ and $A_{T\ sal}$) using a non-zero freshwater endmember ($C_T^{S=0} < 0$, therefore set to 0; $A_T^{S=0}$ = 340 μmol kg^{-1}) according to equation (3) (Friis et al. 2003), with in situ salinity (S) and a reference salinity (S_{ref}) of 34.9 (absolute salinity). The $\Delta C_{T\ sal}$ and $\Delta A_{T\ sal}$ were determined from $C_{T\ sal}$ and $A_{T\ sal}$ by integration between the surface and 120 m depth, as above, and then subtracting these values from the total (ΔC_T and ΔA_T).

$$X_{T\ sal} = ((X_T - X_T^{S=0}/S)' S_{ref}) + X_T^{S=0} \quad (3)$$

Photosynthetic uptake of C_T ($\Delta C_{T\ bio}$; Eqn. 4) was determined from changes in salinity-normalised NO_3 (using the traditional method in Friis et al. (2003)), integrated between the surface and 120 m depth, and applying the Redfield C:N stoichiometric ratio for C:N of 106:16 = 6.6 (Redfield et al. 1963). The Redfield ratio was selected as being representative of average C:N uptake ratios suitable for biological production estimates in Atlantic and Arctic waters in this region (Frigstad et al., 2014; Chierici et al., 2019; (Jones et al., 2021).

$$\Delta T_{T\ bio(surface-120m)} = \Delta NO_{3\ sal(surface-120m)} \times 6.6 \quad (4)$$

Biological uptake of 1 μmol kg^{-1} of C_T during primary production is accompanied by a decrease of 16/106 = ~0.15 μmol kg^{-1} NO_3, which causes an increase in A_T of ~ 0.15 μmol kg^{-1} through the uptake of NO_3 with H^+ to conserve electroneutrality (Brewer and Goldman, 1976). The value for $\Delta A_{T\ bio}$ is therefore estimated from $\Delta C_{T\ bio}$ by applying 0.15 μmol A_T kg^{-1} per 1 μmol C_T kg^{-1} removed during biological production of organic matter (Eqn. (5). Conversely, remineralisation of organic matter from heterotrophic respiration releases increases C_T and NO_3 and decreases A_T with same ratios.

$$\Delta A_{T\ bio(surface-120m)} = \Delta C'_{T\ bio(surface-120m)} - 0.15 \quad (5)$$

The $\Delta C_{T\ CaCO3}$ term accounts for the formation or dissolution of any $CaCO_3$ mineral (biotic aragonite and calcite; abiotic ikaite). Dissolution of $CaCO_3$ produces two bicarbonate ions and consumes one mol of CO_2, thereby increasing A_T by a factor of two relative to the increase in C_T (Zeebe and Wolf-Gladrow, 2001). Formation of $CaCO_3$ affects A_T and C_T negatively by the same 2:1 ratio. Firstly, residual changes in A_T between the surface and 120 m depth are determined by subtracting $\Delta A_{T\ sal}$ and $\Delta A_{T\ bio}$ from ΔA_T, which are ascribed to $CaCO_3$ processes, and then $\Delta C_{T\ CaCO3}$ calculated (Eqn. (6).

$$\Delta C_{T\ CaCO3(surface-120m)} = \Delta A'_{T\ CaCO3(surface-120m)} 0.5 \quad (6)$$

The $\Delta A_{T\ CaCO3}$ and $\Delta C_{T\ CaCO3}$ terms refer to changes due to $CaCO_3$ processes but cannot distinguish which $CaCO_3$ mineral (aragonite, calcite, ikaite) is involved. As $\Delta A_{T\ CaCO3}$ is determined from residual changes from the other ΔA_T terms (Eqn. (2) it may include A_T contributions from other minor sources e.g. mineral weathering, which is assumed to be insignificant in this region (Jones et al., 2021) and errors associated with the other terms.

The $\Delta C_{T\ flux+res}$ term is the difference between ΔC_T and the sum of the other terms ($\Delta C_{T\ sal}$ + $\Delta C_{T\ bio}$ + $\Delta C_{T\ CaCO3}$), which accounts for changes in C_T due to air-sea CO_2 exchange ($\Delta C_{T\ flux}$, section 2.9; uptake or release of 1 mol of CO_2 only affects C_T by an increase or decrease of 1 mol, respectively), residual changes from other processes such as input of CO_2-rich brines, and errors associated with the other ΔC_T terms.

2.7. Net community production

Net community production (NCP; mol C m^{-2}) was estimated at the process (P) stations from changes in salinity-normalised nitrate concentrations ($\Delta NO_{3\ sal}$; μmol kg^{-1}) during the seasonal transitions throughout the growing season: winter/spring (March 2021) and spring (April-May 2021) and summer (August 2019). It was assumed that the replete NO_3 concentrations in the well-mixed water column in winter/spring (March 2021) were representative of pre-bloom conditions in order to estimate NCP by summer of a different year, i.e. August 2019. The $\Delta NO_{3\ sal}$ was integrated in the upper 50 m of the water column and converted to carbon using C:N stoichiometric ratio 106:16 (Redfield et al., 1963), as described above for determining $\Delta C_{T\ bio}$ in the upper

120 m. The upper 50 m depth range was selected for the NCP estimates as this depth was below the typical mixed layer depth and within the nitracline in summer for this region (Koenig et al., this issue b; Renner et al., this issue), and for comparisons to other NCP estimates in the Atlantic Water inflow and Barents Sea (Assmy et al., 2017; Fransson et al., 2017; Chierici et al., 2019).

2.8. Ocean acidification state

Values of Ωaragonite and Ωcalcite and the A_T:C_T ratio (in situ values of A_T relative to C_T) can be used as indicators of the ocean acidification state in relation to changes in C_T (ΔC_T) and A_T (ΔA_T) in the upper 120 m driven by the processes discussed in section 2.6. Changes in C_T and A_T affect Ω; increased C_T and decreased A_T suppresses Ω and decreased C_T and increased A_T enhances Ω. The Ω was calculated from input pairs of C_T and A_T (Q3, Q1, Q2) and C_T and pH (Q4) with in situ temperature, salinity, pressure and concentrations of PO_4 and $Si(OH)_4$ using the chemical speciation model CO2SYS (Pierrot et al., 2006). The carbonic acid dissociation constants of Mehrbach et al. (1973), as refitted by Dickson and Millero (1987), were used with the bisulfate dissociation constant from Dickson (1990) and the total boron concentration of Lee et al. (2010). The aragonite and calcite stoichiometric solubility constants of Mucci (1983) were used with the pressure corrections of Millero (1979) and the $CaCO_3$ and salinity ratio of Riley and Tongudai (1967). When $\Omega < 1$ the seawater is undersaturated with respect to $CaCO_3$ and $CaCO_3$ minerals are vulnerable to dissolution. Discussions on

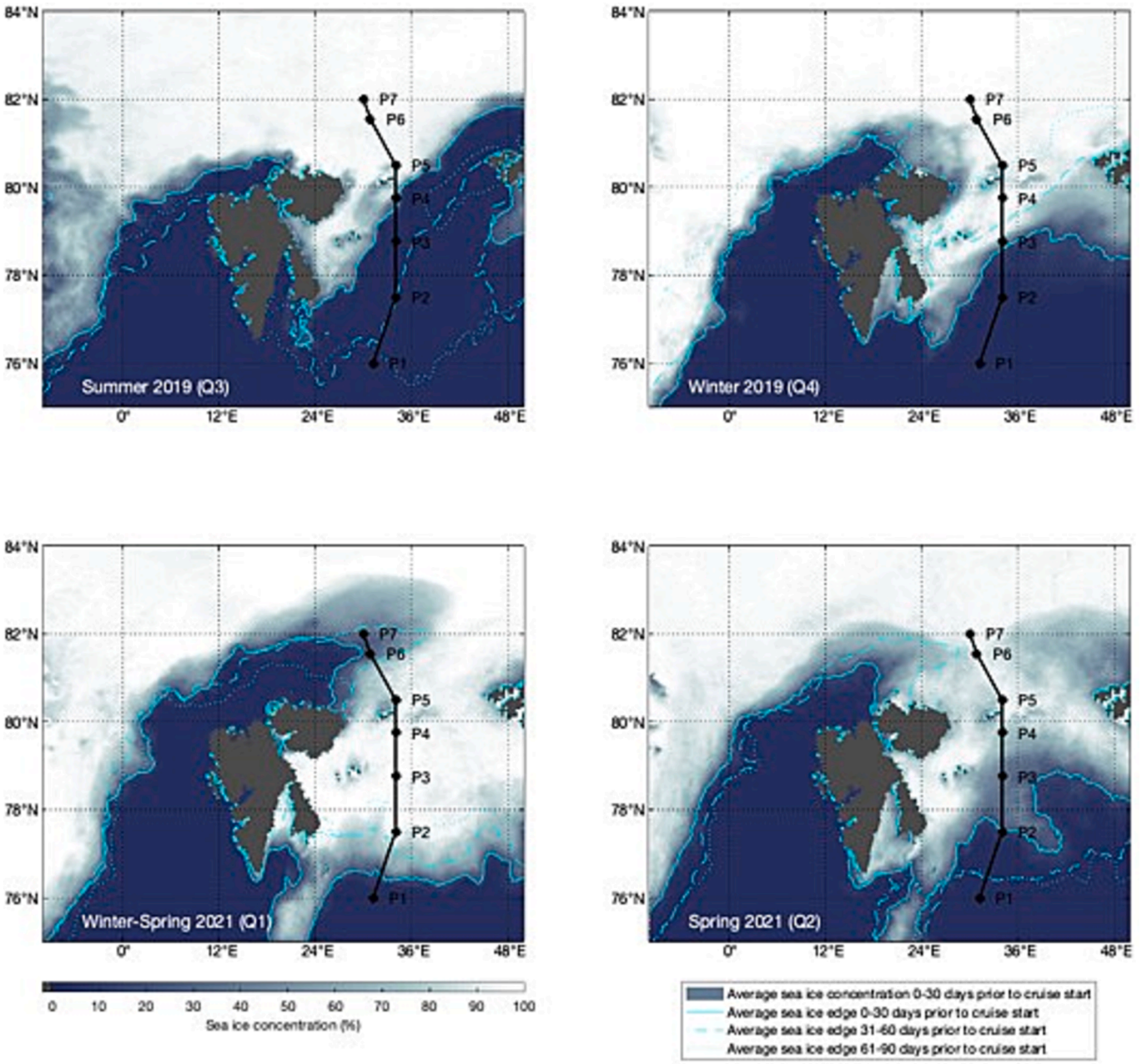

Fig. 2. Sea-ice conditions during summer (August 2019), winter (December 2019), winter/spring (March 2021) and spring (April-May 2021). The locations of the main process (P) stations are shown. Average sea ice concentration (%) is shown (shading) with average location of the ice edge at 0–30 days (solid cyan line), 31–60 days (dashed cyan line) and 61–90 days (dotted cyan line) indicated. Sea ice concentration data derived from AMSR-2 was downloaded from the Institute of Environmental Physics, University of Bremen, Germany (Spreen et al., 2008). (For interpretation of the references to colour in this figure legend, the reader is referred to the web version of this article.)

the state of ocean acidification will focus on Ωaragonite as aragonite is the more unstable biotic $CaCO_3$ mineral.

2.9. Air-sea CO_2 fluxes

Air-sea CO_2 fluxes were calculated from the air-sea gradient in the fugacity of CO_2 (ΔfCO_2sea-air) following the procedure described in Jones et al. (2021). The fCO_2 in surface water was calculated from input pairs of C_T and A_T (Q3, Q1, Q2) and C_T and pH (Q4) with using the chemical speciation model CO2SYS as described in section 2.8. The atmospheric mixing ratio of CO_2 (xCO_2) was obtained from the Zeppelin Observatory, Spitsbergen (78.907 °N, 11.888 °E) and was converted to fCO_2 following Dickson et al. (2007) and Ericson et al., 2023, and references therein. Seasonal mean wind speeds (mean value of observations from 3 months prior to each seasonal cruise) were obtained from the Verlegenhuken weather station, Spitsbergen (80.056 °N, 16.243 °E), from https://seklima.met.no/observations/. Sea ice concentrations at the location of each hydrographic station (Fig. 2) were estimated from daily sea ice concentration data, as reported in Van Engeland et al. (2023), and were used to determine ice-scaled CO_2 fluxes (assuming 100 % sea ice cover limits significant air-sea CO_2 exchange).

A negative air-sea CO_2 flux indicates oceanic uptake of CO_2, increasing C_T in the surface layer, and that the ocean is a sink for atmospheric CO_2. To account for the effects of CO_2 uptake on changes in C_T in the surface layer ($\Delta C_{T\ flux}$) the corresponding total change in C_T (mol m^{-2} per season) was calculated using the daily ice-scaled fluxes summed for the 3 months (average 90 days) to represent each season. The $\Delta C_{T\ flux}$ in the surface layer is compared to integrated changes in the upper 120 m due to air–sea CO_2 fluxes and residual effects ($\Delta C_{T\ flux+res}$), as described in section 2.6.

2.10. Uncertainties in analytical techniques and calculations

Uncertainties associated with the total ΔC_T (Eqn. (1) and ΔA_T (Eqn. (2) were based on the analytical precision of the measurements (±2 μmol kg^{-1}) and estimated (square-root-of-sum-of-squares of the absolute errors) as ± 3 μmol kg^{-1}. Similarly, uncertainties in $\Delta C_{T\ sal}$ and $\Delta A_{T\ sal}$ were ± 3 μmol kg^{-1}. Uncertainties in $\Delta C_{T\ bio}$ and $\Delta A_{T\ bio}$ were estimated from the combination of analytical precision for NO_3 and deviations in the C:N ratio (Redfield et al., 1963; Frigstad et al., 2014). An upper bound of the error for $\Delta NO_{3\ sal}$ was ± 0.1 μmol kg^{-1}, corresponding to errors $C_{T\ bio}$ ± 1 μmol kg^{-1} and variability in C:N of ± 1 μmol kg^{-1}, yielding composite uncertainties for $\Delta C_{T\ bio}$ ± 2 μmol kg^{-1} and $\Delta A_{T\ bio}$ ± 1 μmol kg^{-1}. Upper bound uncertainties in $\Delta A_{T\ CaCO3}$ and $\Delta C_{T\ CaCO3}$ were estimated from combined uncertainty as ± 4 μmol kg^{-1}. Associated errors on $\Delta C_{T\ flux+res}$ are estimated as ± 4 μmol kg^{-1}.

3. Results

3.1. Sea ice and hydrography

The northern Barents Sea and Nansen Basin were ice covered during all seasons (Fig. 2), varying from minimum ice cover in summer (August 2019) to maximum ice cover in winter (March 2021) with the ice edge indicating the MIZ. The variations in conservative temperature and absolute salinity (Fig. 3) and potential density characterises (Table 2) identified key water masses in the water column (Fig. 4). During all seasons, Atlantic Water, warm Polar Water and modified Atlantic Water dominated the water column south of the Polar Front at P1 (Fig. 3 – 4). Shoaling of isotherms and isohalines to the surface marked the influence of Atlantic Water along the northern shelf, which was most pronounced in winter (December 2019). Eurasian Basin Deep Water (EBDW) was identified during each season at about 1500–3500 m in the Nansen Basin. The definition of EBDW overlaps with that of Intermediate Water (IW) in Sundfjord et al. (2020), which will be referred to hereafter as IW/EBDW and was found at 800–1500 m depth in the Nansen Basin. The IW/EBDW likely has Intermediate Water as a source water mass but has been isolated from the atmosphere and accumulated over multiple years or decades whereas Intermediate Water on the Barents Sea shelf exhibited seasonal signals from wintertime ventilation and accumulation of saline brines from forming sea ice.

In summer (August 2019), sea ice was present across the shelf of the Barents Sea with the ice edge located north of 79.75°N and east of 34°E between P4 and P5 (Fig. 2). Warm Polar Water occupied the upper layer (10–45 m depth) from P2 to P4 with an underlying layer of Polar Water (Fig. 3a, 4). In the deepest layers, Intermediate Water was found at P2 and cold, dense CBSDW was found across the central shelf from P3 to P4 (Fig. 4). The whole water column around P5 was dominated by Polar Water. Around P6 on the shelf and northwards to P7 in the Nansen Basin, colder and fresher Polar Water defined the surface layer, with underlying warm Polar Water, Atlantic Water and modified Atlantic Water at increasing depth. By winter (December 2019), sea ice cover extended southwards with the ice edge located at around P3 (Fig. 2). The water column at P1 was warmer and more saline compared with summer, with modified Atlantic Water found in the deepest layer (Fig. 3b, 4). The ice-covered water column north of P2 was predominantly colder and fresher Polar Water. Warm Polar Water re-emerged at around P5 and towards P6 in the deeper layers. Atlantic Water was identified by a more pronounced warm core between ~ 150 and 210 m depth from P6 to P7.

Winter/spring (March 2021) was characterised by the seasonal maximum in sea ice cover, with the ice edge located between P1 and P2 (Fig. 2). The ice-free and well mixed water column at P1 was occupied by modified Atlantic Water (Fig. 3c, 4). Polar Water with underlying warm Polar Water characterised the water column from P2 to around P4. The whole water column at P5 was dominated by Polar Water. Below the surface Polar Water layer north of P5, warm Polar Water and modified Atlantic Water were identified in mid (50–200 m) and deep (490–840 m) depth ranges, respectively. North of the shelf break, Atlantic Water was only found at P6 at around 500 m depth. Intermediate Water occupied the deep (1000–3370 m) layers from P6 to P7. No Intermediate Water or CBSDW was detected over the Barents Sea shelf. Recent decreasing and increasing sea ice cover was evident between P6 and P7, which coincided with warm Polar Water intruding the surface layer (Fig. 3c). By spring (April-May 2021), the onset of seasonal sea ice retreat was evident by the more northerly location of the ice edge around P2 (Fig. 2). P1 remained well mixed with modified Atlantic Water (Fig. 3d). The seasonal sea ice melt influenced the water column with cold and fresh Polar Water at all depths north of the Polar Front to P3 (Fig. 3d, 4). Across the shelf from P3 to around P6, warm Polar Water was found in the deeper layers, with the exception of P5 where Polar Water was present at all depths (same as observed during summer and winter/spring). North of P6, modified Atlantic Water was found in deeper (750–900 m) layers and no Atlantic Water was identified north of the shelf break. No Intermediate Water or CBSDW was detected over the Barents Sea shelf in 2021.

3.2. Inorganic nutrients and carbonate chemistry

In summer (August 2019), depleted NO_3, PO_4 and $Si(OH)_4$ characterised much of the upper layers of Polar Water and warm Polar Water (Fig. 5, S1). Concentrations increased with depth to Intermediate Water overlying the shelf (150–200 m depth) and IW/EBDW in the deep Nansen Basin, where highest NO_3 and $Si(OH)_4$ concentrations of ~ 15 and ~ 12 μmol kg^{-1}, respectively, were found (Table 2). Lowest A_T (2134 μmol kg^{-1}) and C_T (1930 μmol kg^{-1}) were found in the surface Polar Water layer (Fig. 6). Values of A_T and C_T increased with depth to highest A_T (2317 μmol kg^{-1}) in Atlantic Water (at P1) and highest C_T (2203 μmol kg^{-1}) in Intermediate Water (at P2) over the shelf (Table 2). Deepest layers over parts of the shelf that were occupied by CBSDW (around P3 and P4) showed reductions in NO_3, and similar values of $Si(OH)_4$ and A_T, and increased C_T, relative to the overlying Polar Water

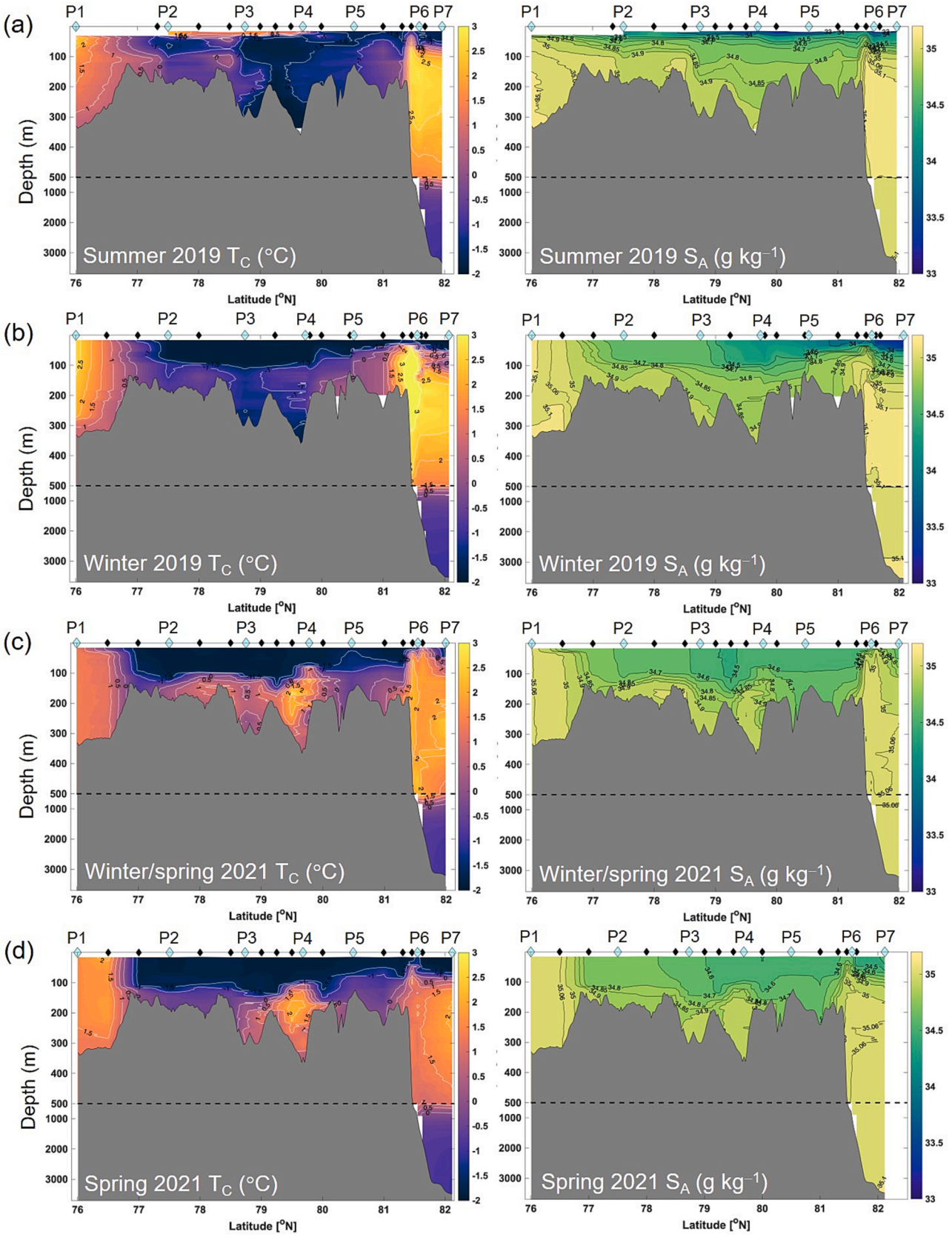

Fig. 3. Transect section plots of conservative temperature (T_C; °C) and absolute salinity (S_A; g kg^{-1}) during (a) summer (August 2019), (b) winter (December 2019), (c) winter/spring (March 2021) and (d) spring (April-May 2021). The locations of the hydrographic stations (black diamonds) and process (P) stations (blue diamonds) are marked and labelled. The y-axis is expanded in the upper 500 m. (For interpretation of the references to colour in this figure legend, the reader is referred to the web version of this article.)

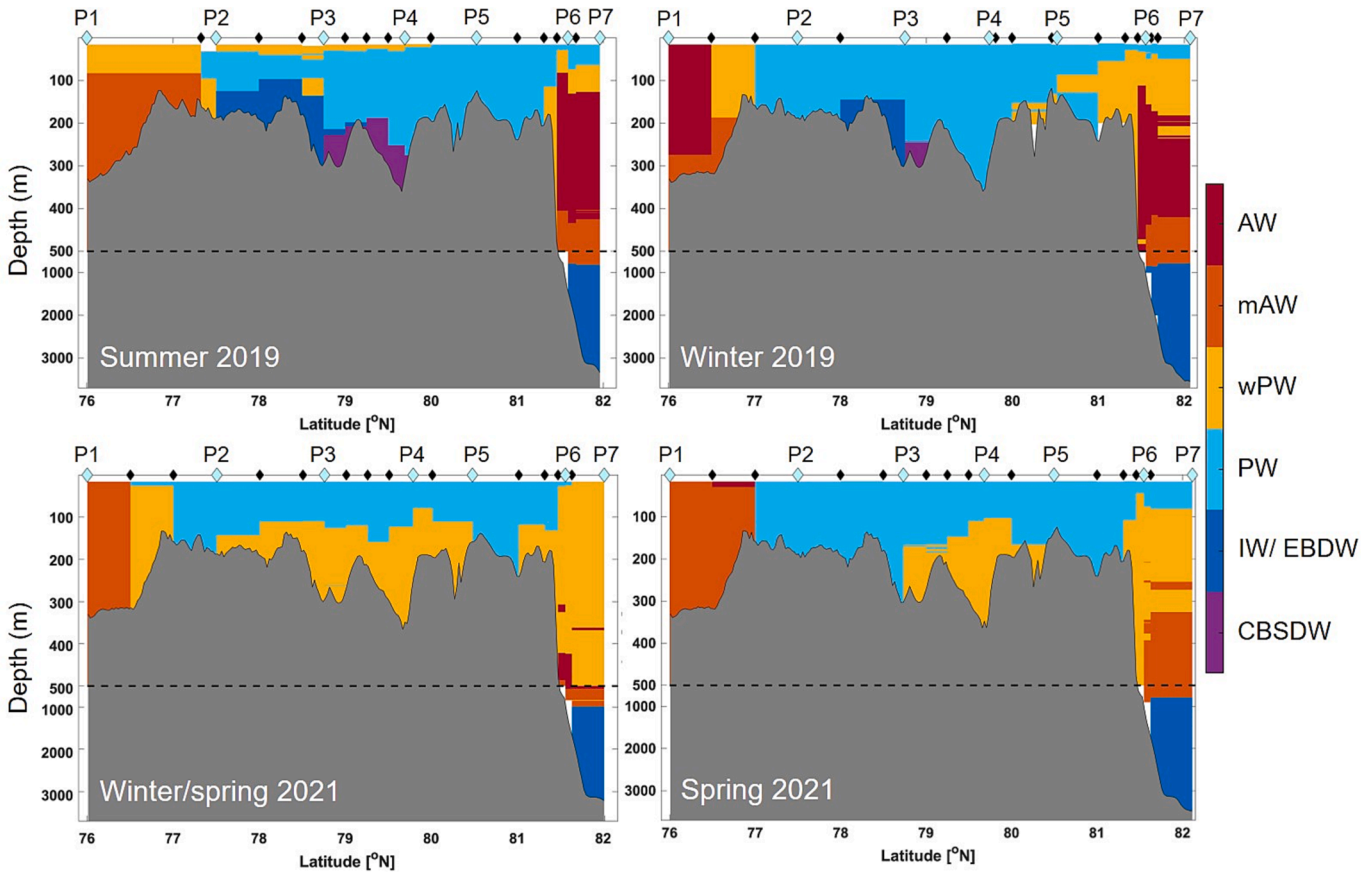

Fig. 4. Water mass distribution during summer (August 2019), winter (December 2019), winter/spring (March 2021) and spring (April-May 2021) colour-coded to identify Warm Polar Water (wPW), Polar Water (PW), Atlantic Water (AW), Modified Atlantic Water (mAW), Intermediate Water (IW), Cold Barents Sea Dense Water (CBSDW) and Eurasian Basin Deep Water (IW/ EBDW). The locations of the hydrographic stations (black diamonds) are marked and process (P) stations (blue diamonds) are marked and labelled. The y-axis is expanded in the upper 500 m. (For interpretation of the references to colour in this figure legend, the reader is referred to the web version of this article.)

(Fig. 5). Lowest average surface layer A_T occurred in the Polar Water (Table 2). The water column at and around P5 was dominated by Polar Water with low A_T and C_T and exhibited little variability for all seasons. By winter (December 2019), the water column was becoming replenished with nutrients and with higher A_T and C_T south of the ice edge, with an imprint of summer meltwater inputs and primary production in the surface layer (Fig. 5 – 6). Nutrients, C_T and A_T generally increased with depth to the Intermediate Water, except for decreases in CBSDW (at P3 and P4). High C_T in Polar Water and Intermediate Water occurred at and around P2. Compared with the other seasons, Atlantic Water concentrations of NO_3 and $Si(OH)_4$ were generally lowest in winter.

In winter/spring (March 2021), the well-mixed water column was relatively homogenous and rich in nutrients and C_T and with higher A_T (Fig. 5 – 6, S1). Relative to all seasons, highest average values in warm Polar Water of NO_3, A_T and C_T and Polar Water concentrations of NO_3, A_T and C_T occurred (Table 2). Highest average values of Atlantic Water concentrations of NO_3, $Si(OH)_4$ and C_T also occurred during winter/spring. Highest average NO_3 ~ 15 μmol kg^{-1} and $Si(OH)_4$ ~ 13 μmol kg^{-1} concentrations were found in IW/EBDW in the Nansen Basin (Table 2). By spring (April-May 2021), the water column was still largely homogenous, nutrient replete and with high A_T and C_T (Fig. 5 – 6, S1). Nutrient concentrations were similar in the surface and Atlantic Water layers, increased in Intermediate Water and A_T and C_T were highest (A_T ~ 2313 μmol kg^{-1}; C_T ~ 2184 μmol kg^{-1}) in the Atlantic Water layers. Values for NO_3, C_T and A_T were slightly reduced in the surface layer compared with winter/spring. In contrast, $Si(OH)_4$ in warm Polar Water and Polar Water were the highest in all seasons (Fig. 5b; Table 2).

3.3. Biogeochemical-physical coupling and ocean acidification state

For each season, variability in A_T and C_T in the water column is closely linked to the distribution to different water masses that exhibit different A_T and C_T and thus varying A_T:C_T from physical, biogeochemical and biological processes. Largest variations in A_T and C_T during summer coincided with a wider range of salinities from inputs of fresh sea-ice meltwater (Fig. 7a). The variability in A_T was more closely coupled to salinity as expected from the near-conservative behaviour of A_T, showing lower A_T in low salinity Polar Water and higher A_T with saline Atlantic Water. Increased variability in C_T shows effects of other processes driving changes in C_T, particularly in summer.

The Ωaragonite varied between 0.76 and 2.30 in the full water column across all seasons controlled by changes in A_T and C_T, as reflected in the A_T:C_T ratio that ranged between 1.04 and 1.12 with effects of temperature (coldest and low Ωaragonite in winter/spring) and pressure (high pressure and low Ωaragonite in the deep Nansen Basin). Generally high Ωaragonite (mean 1.57–1.76) occurred in the surface warm Polar Water and Polar Water layers in summer, driven by reduced C_T (Table 2; Fig. 7b). Highest Ωaragonite of 2.25–2.30, and most buffered waters with mean A_T:C_T up to 1.08, occurred in warm Polar Water (at P1). The saline and high-A_T Atlantic Water and modified Atlantic Water typically had high Ωaragonite with seasonal mean values of 1.34–1.64 and moderate buffer capacity with mean A_T:C_T of 1.06–1.07. Over the Barents Sea shelf, dense and cold CBSDW had Ωaragonite around 1.23 and had low buffer capacity (mean A_T:C_T ratio of 1.05) driven by elevated C_T in summer and winter. Generally low Ωaragonite of 1.12–1.14 (mean A_T:C_T ratio of 1.04–1.05) was found at 150–180 m in

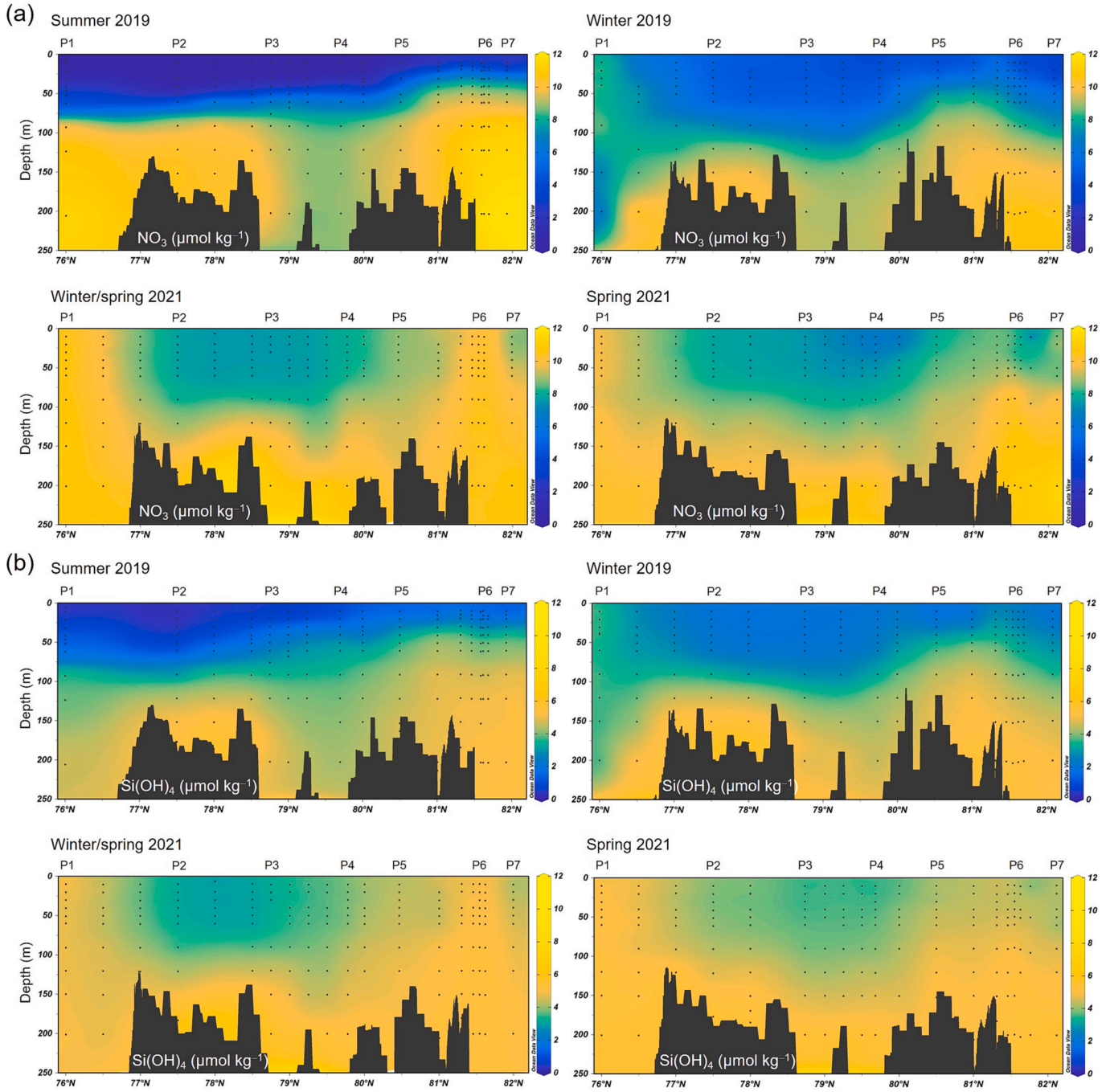

Fig. 5. Transect section plots of (a) NO_3 (µmol kg^{-1}) and (b) silicic acid ($Si(OH)_4$) (µmol kg^{-1}) in the upper 250 m during summer (August 2019), winter (December 2019), winter/spring (March 2021) and spring (April-May 2021). The locations of the process (P) stations are labelled. Ocean Data View was used for data visualisation (Schlitzer, 2022).

the lower-A_T and higher-C_T Polar Water and Intermediate Water (at and around P2) in summer and winter. Aragonite undersaturation and lowest Ωaragonite of 0.76–0.78 occurred at 2800–3600 m in the lower-A_T and nutrient-rich IW/EBDW in the Nansen Basin (at and around P7).

All water column nutrient and C_T data yielded close coupling and significant relationships between the cycling of C_T and NO_3, NO_3 and PO_4, and $Si(OH)_4$ and NO_3 (Table 3; Fig. 8). Nutrient uptake ratios for C:N (Fig. 8a) ranged from highest values of 10.3 ± 0.6 in summer to lowest of 2.6 ± 0.4 in winter/spring. Uptake ratios for N:P (Fig. 8b) ranged from 17.2 ± 0.3 in winter/spring to 16.3 ± 0.3 in winter. Uptake ratios for Si:N (Fig. 8c) ranged from 0.94 ± 0.03 in winter/spring to 0.50 ± 0.02 in summer. These inorganic carbon and nutrient ratios reveal different stoichiometry between the seasons.

3.4. Seasonal changes in C_T and A_T

3.4.1. Seasonality and effects on ocean acidification state

Seasonal variability in C_T and A_T in the whole water column can be illustrated using theoretical trend lines to depict the impact of key processes, with potential synergy, and on the ocean acidification state, Ωaragonite (Fig. 9). Salinity-normalising C_T and A_T ($C_{T\ sal}$ and $A_{T\ sal}$) removes variability in C_T and A_T that result from salinity changes through physical processes, such as freshwater inputs, advection and mixing. The variability that remains in the $A_{T\ sal} - C_{T\ sal}$ space results

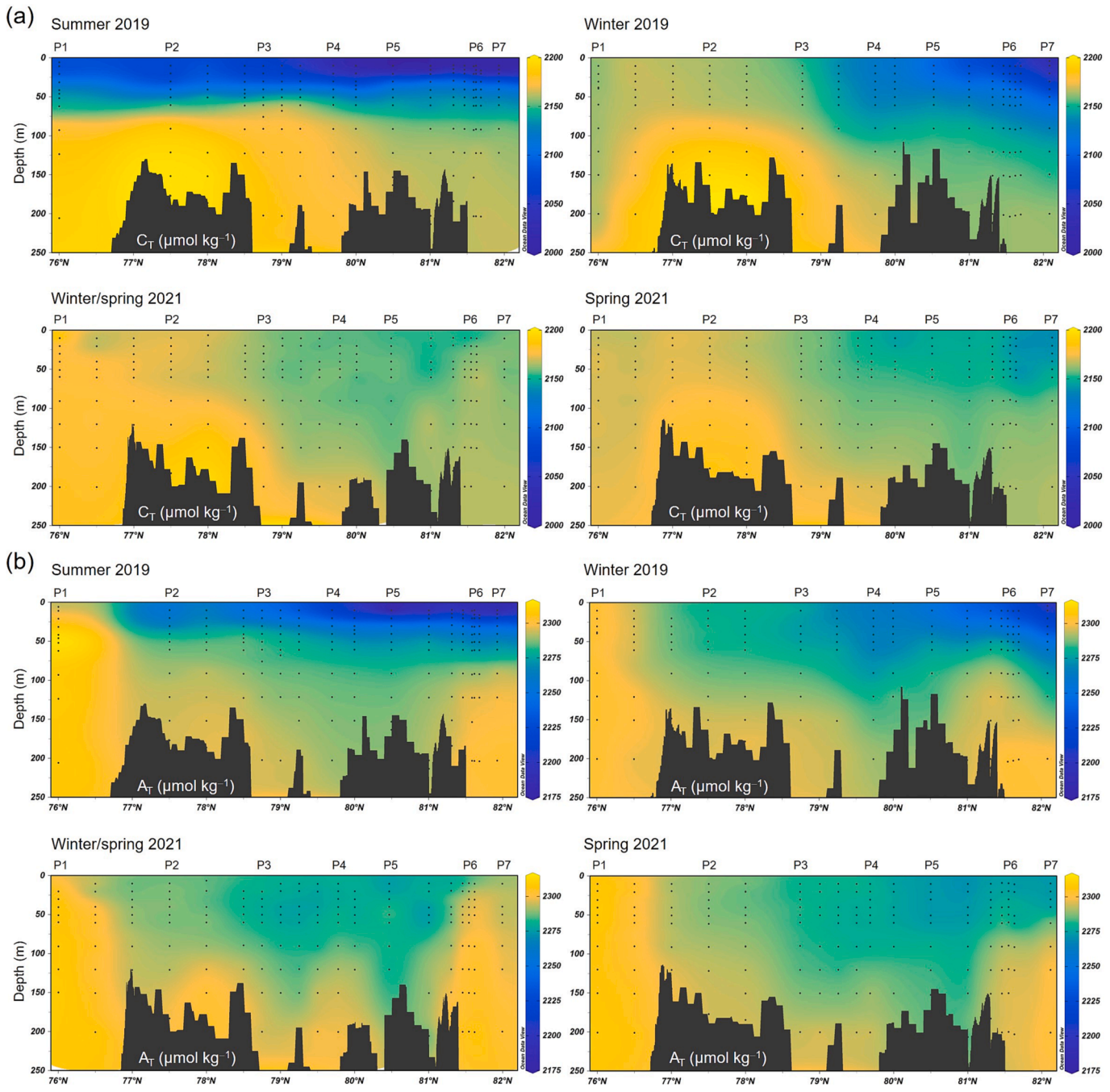

Fig. 6. Transect section plots of (a) C_T (µmol kg^{-1}) and (b) A_T (µmol kg^{-1}) in the upper 250 m during summer (August 2019), winter (December 2019), winter/spring (March 2021) and spring (April-May 2021). The locations of the process (P) stations are labelled. Ocean Data View was used for data visualisation (Schlitzer, 2022).

from biological processes of primary production and organic matter remineralisation (respiration) and biogeochemical processes, such as $CaCO_3$ formation/dissolution and air-sea CO_2 uptake/release.

Primary production reduced $C_{T\ sal}$, with slight increases in $A_{T\ sal}$, in summer, associated with elevated Ωaragonite > 1.8. The imprint of biological processes on $C_{T\ sal}$ likely contributed to the variability observed in the following winter (pre-conditioned from the growing season) and also in spring (at the start of the spring bloom). Remineralisation of organic matter contributed to higher values of $C_{T\ sal}$, associated with lower Ωaragonite < 1.4, during the seasonal transitions. Reduced $A_{T\ sal}$ and $C_{T\ sal}$ in summer may also result from formation of biotic $CaCO_3$ by calcifiers in the water column. Increased $A_{T\ sal}$ and $C_{T\ sal}$ and higher Ωaragonite could include contributions from dissolution of biotic $CaCO_3$ and abiotic $CaCO_3$ (ikaite). Reduced $A_{T\ sal}$ and $C_{T\ sal}$ and lower Ωaragonite from winter/spring to spring could include a signal of ikaite formation in sea ice. The relative increase in $C_{T\ sal}$ at constant $A_{T\ sal}$ could result from atmospheric CO_2 uptake in ice-free surface waters from summer to winter to spring due to an increase in CO_2 solubility in cooler surface waters (decreased Ωaragonite).

3.4.2. Seasonal drivers in the upper ocean

The value of ΔC_T and ΔA_T represent 100 % of the total change as the sum of all seasonal drivers of C_T ($\Delta C_{T\ sal} + \Delta C_{T\ bio} + \Delta C_{T\ CaCO3} + \Delta C_{T\ flux+res}$) and A_T ($\Delta A_{T\ sal} + \Delta A_{T\ bio} + \Delta A_{T\ CaCO3}$) changes, thus the absolute value of each term is taken to represent a fraction (%) of ΔC_T and ΔA_T, irrespective of the direction of change. The main driver of C_T and A_T changes from the surface layer to 120 m depth was salinity changes that accounted on average for 37–55 % of ΔC_T and 78–85 % of ΔA_T

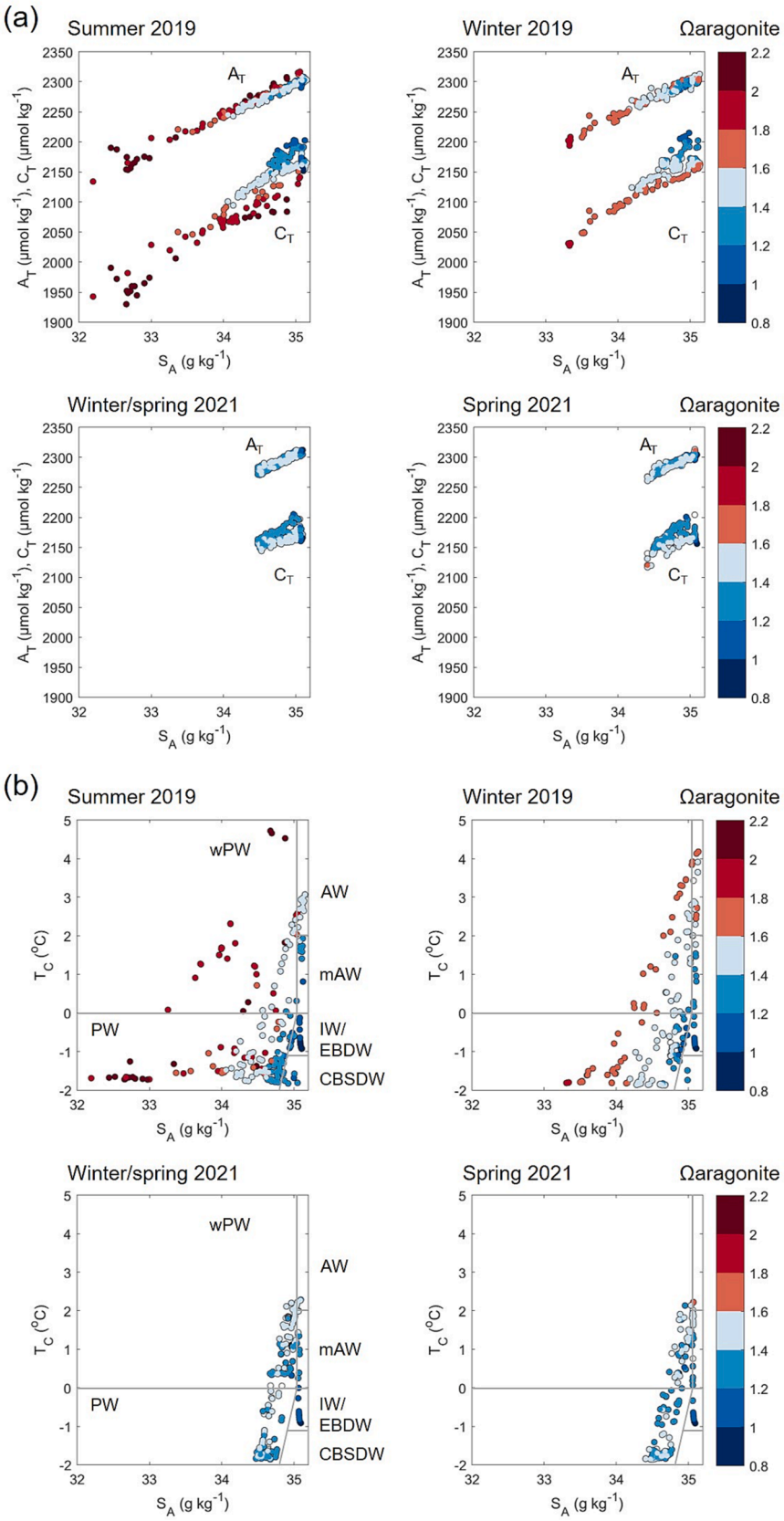

Fig. 7. Relationships between (a) A_T and C_T (µmol kg^{-1}) and salinity (S_A; g kg^{-1}) and (b) temperature (T_C: °C) and salinity (S_A; g kg^{-1}) during summer (August 2019), winter (December 2019), winter/spring (March 2021) and spring (April-May 2021). Data are coloured by Ωaragonite. Water masses warm Polar Water (wPW), Polar Water (PW), Atlantic Water (AW), modified Atlantic Water (mAW), Intermediate Water (IW), Eurasian Basin Deep Water (EBDW) and Cold Barents Sea Dense Water (CBSDW) are labelled in (b).

Table 3
Linear regression relationships for inorganic carbon (C), nitrate (N), phosphate (P) and silicic acid (Si) in the full water column for each season; summer (August 2019), winter (December 2019), winter/spring (March 2021) and spring (April-May 2021). Regression analysis information determined with Matlab (version 2017b) linear regression model fitlm: gradient ± standard error (se), r^2, p value (statistically significant if $p \leq 0.05$) and n number of observations.

Linear regression	Season (year)	Gradient ± se	r^2	p	n
C:N	Summer (2019)	10.3 ± 0.6	0.59	< 0.01	200
	Winter (2019)	7.3 ± 0.7	0.38	< 0.01	178
	Winter/spring (2021)	2.6 ± 0.4	0.18	< 0.01	182
	Spring (2021)	2.9 ± 0.5	0.18	< 0.01	190
N:P	Summer (2019)	16.8 ± 0.2	0.97	≪ 0.01	200
	Winter (2019)	16.3 ± 0.3	0.96	≪ 0.01	176
	Winter/spring (2021)	17.2 ± 0.3	0.96	≪ 0.01	190
	Spring (2021)	17.0 ± 0.2	0.96	≪ 0.01	188
Si:N	Summer (2019)	0.50 ± 0.02	0.76	< 0.01	200
	Winter (2019)	0.73 ± 0.03	0.81	< 0.01	204
	Winter/spring (2021)	0.94 ± 0.03	0.83	< 0.01	191
	Spring (2021)	0.81 ± 0.03	0.83	< 0.01	191

during all seasons (Fig. 10). Changes due to primary production/respiration accounted for an average of 23–37 % of ΔC_T accompanied by change of 8–12 % of ΔA_T. Formation/dissolution of $CaCO_3$ represented an average 5–13 % of ΔA_T with associated 1–3 % of ΔC_T.

For $\Delta C_{T\ flux+res}$, air-sea CO_2 fluxes potentially represented an average of 4–37 % of ΔC_T, which also included residual changes (e.g. input of CO_2-rich brines from sea ice) and uncertainties from the other ΔC_T terms. Surface waters were undersaturated in CO_2 relative to the atmosphere in all seasons (Fig. S3a), with strong undersaturation persisting in the Nansen Basin. Ice-scaled CO_2 fluxes generally showed increased CO_2 uptake, corresponding to higher $\Delta C_{T\ flux}$, in surface waters south of the seasonal ice edge, and less CO_2 uptake and thus lower $\Delta C_{T\ flux}$ in ice-covered waters over the slope and in the Nansen Basin (Fig. S3b – c). From average $\Delta C_{T\ flux}$ values across the Atlantic and Arctic regimes (Fig. S3), surface waters were an annual CO_2 sink. Higher $\Delta C_{T\ flux+res}$ values in all seasons occurred beneath the sea ice, implying input of CO_2 from other processes, e.g. from sea-ice brines, and that uncertainties in the other terms likely increased in ice-influenced waters.

Summer (August 2019) exhibited the largest ΔC_T and ΔA_T that coincided with the sea-ice cover. The main drivers were salinity changes (56 % of ΔC_T; 83 % of ΔA_T) and primary production (37 % of ΔC_T; 9 % of ΔA_T) following the seasonal ice melt and growing season. Highest ΔC_T of − 13.1 mol m^{-2} and highest ΔA_T of − 8.5 mol m^{-2} occurred over the central shelf (around P5). Sea-ice meltwater diluted A_T and C_T in the with $\Delta A_{T\ sal}$ of − 8.2 mol m^{-2} and $\Delta C_{T\ sal}$ of − 8.9 mol m^{-2} over the shelf (P5). Primary production was the main driver south of the ice edge, with $\Delta C_{T\ bio}$ of − 4.3 mol m^{-2} ($\Delta A_{T\ bio}$ of 0.7 mol m^{-2}) south of the Polar Front (P1). Formation/dissolution of biotic and/or abiotic $CaCO_3$ accounted for on average 3 % of ΔC_T and 10 % of ΔA_T, with $\Delta A_{T\ CaCO3}$ up to 1.4 mol m^{-2} ($\Delta C_{T\ CaCO3}$ of 0.7 mol m^{-2}) beneath the sea ice. Changes due to air-sea CO_2 fluxes and residual changes accounted for ~ 5 % of ΔC_T and varied from loss of C_T with $\Delta C_{T\ flux+res}$ of − 1.4 mol m^{-2} over the slope to inputs of C_T with $\Delta C_{T\ flux+res}$ of 2.3 mol m^{-2} over the shelf. The ΔfCO_2 values exhibited strong seasonality with substantial CO_2 undersaturation in surface waters with ΔfCO_2 around − 250 µatm in summer (Fig. S3). Ice-scaled $\Delta C_{T\ flux}$ showed maximum seasonal atmospheric CO_2 uptake of 0.7–0.9 mol m^{-2} in ice-free surface waters (Fig. S3b – c).

By winter (December 2019), changes due to salinity change remained the main driver (45 % of ΔC_T; 78 % of ΔA_T) with an imprint of summertime primary production (31 % of ΔC_T; 9 % of ΔA_T) being eroded with increasing respiration/remineralisation (Fig. 10). A shift to positive ΔC_T and a net increase in C_T of 0.2 mol m^{-2} occurred just north of the Polar Front. Salinity-driven changes were diminished relative to summer, with $\Delta A_{T\ sal}$ of − 4.9 mol m^{-2} and $\Delta C_{T\ sal}$ of − 5.3 mol m^{-2} in the Nansen Basin. Respiration reduced the summer C_T-uptake signal with $\Delta C_{T\ bio}$ of around − 2.6 mol m^{-2} in the Nansen Basin. The contribution from $CaCO_3$ processes accounted for 3 % of ΔC_T and 13 % of ΔA_T with $\Delta A_{T\ CaCO3}$ between − 0.5 mol m^{-2} to 0.2 mol m^{-2} over the shelf. Wintertime $\Delta C_{T\ flux+res}$ showed a general shift to net increases in C_T accounting for up to 21 % with highest $\Delta C_{T\ flux+res}$ of 1.9 mol m^{-2}. Ice-scaled $\Delta C_{T\ flux}$ showed atmospheric CO_2 uptake up to 0.5 mol m^{-2} in surface waters south of the ice edge (Fig. S3).

In winter/spring (March 2021), salinity changes (39 % of ΔC_T; 85 % of ΔA_T) was the dominant driver (Fig. 10) The well mixed water column had seasonally low ΔC_T and ΔA_T of − 1.5 mol m^{-2} and − 2.1 mol m^{-2}, respectively, and slight positive ΔC_T and ΔA_T over the central shelf. $\Delta C_{T\ sal}$ and $\Delta A_{T\ sal}$ were more variable with $\Delta C_{T\ sal}$ ranging between − 1.8 and 0.0 mol m^{-2} and $\Delta A_{T\ sal}$ ranging between − 1.6 and 0.0 mol m^{-2}. Largest $\Delta C_{T\ sal}$ and $\Delta A_{T\ sal}$ occurred with varying sea-ice cover in the slope and Nansen Basin. $\Delta C_{T\ bio}$ was seasonally low ranging between − 1.2 and 0.0 mol m^{-2} (23 % of ΔC_T). The $\Delta A_{T\ CaCO3}$ was seasonally low (6 % of ΔA_T) ranging between − 0.7 mol m^{-2} over the shelf and 0.4 mol m^{-2} in the Nansen Basin. By late spring (April-May 2021), the main driver was salinity changes (37 % of ΔC_T; 84 % of ΔA_T) alongside contributions from primary production (31 % of ΔC_T; 12 % of ΔA_T). Similar to winter/spring, smaller seasonal ΔC_T of − 1.9 mol m^{-2} and ΔA_T of − 1.7 mol m^{-2} occurred with positive ΔC_T and ΔA_T over the central shelf. The ranges of $\Delta C_{T\ sal}$ and $\Delta A_{T\ sal}$ increased, with greatest changes with $\Delta C_{T\ sal}$ of − 2.0 and $\Delta A_{T\ sal}$ of − 2.1 mol m^{-2} in the Nansen Basin. The onset of the spring bloom decreased C_T with $\Delta C_{T\ bio}$ of − 1.3 mol m^{-2} in the central shelf. The $\Delta A_{T\ CaCO3}$ remained seasonally low (1 % of ΔC_T; 5 % of ΔA_T), ranging between − 0.5 mol m^{-2} as a signal of $CaCO_3$ formation and 0.6 mol m^{-2} as a signal of $CaCO_3$ dissolution over the central shelf. In winter/spring and spring, the $\Delta C_{T\ flux+res}$ ranged between − 0.3 and 1.7 mol m^{-2} and accounted for 32–37 % of ΔC_T. The ΔfCO_2 values were minimum around − 50 µatm in winter/spring and ice-scaled $\Delta C_{T\ flux}$ showed atmospheric CO_2 uptake in surface waters south of the ice edge was up to 0.5–0.6 mol m^{-2} (Fig. S3).

3.5. Net community production

Estimates of NCP from changes in NO_3 in the upper 50 m from winter/spring to spring (NCP_{spr}) showed that some biological carbon uptake had occurred by the spring but higher NCP from winter/spring to summer (NCP_{sum}) occurred across the Atlantic and Arctic regimes (Table 4). There was a general northward decrease in NCP_{sum} from 1.3 mol C m^{-2} (14 g C m^{-2}) at P1 to 0.4 mol C m^{-2} (5 g C m^{-2}) at P7. The highest NCP_{spr} was 0.3 mol C m^{-2} at P6.

3.6. Interannual variability

With a one-year gap between the seasonal cruises in 2019 and 2021, year-to-year variations were superimposed onto the seasonal changes in the northwestern Barents Sea. The Barents Sea shelf and slope, Atlantic Water inflow and adjoining Nansen Basin exhibit strong interannual variability in sea ice and hydrographic conditions (Lundesgaard et al., 2022; Renner et al., this issue).

A strong seasonal cycle in sea-ice cover and temperature in the surface layer and in deeper waters in the southern part of the shelf (P2) persisted throughout 2019–2021 (Van Engeland et al., 2023). The variability in the surface layer in the central region (P4) showed a relatively regular seasonal pattern throughout 2019–2021, however year-to-year variations were evident in deeper waters during this period (Van Engeland et al., 2023) that resulted in shifts between cold IW and

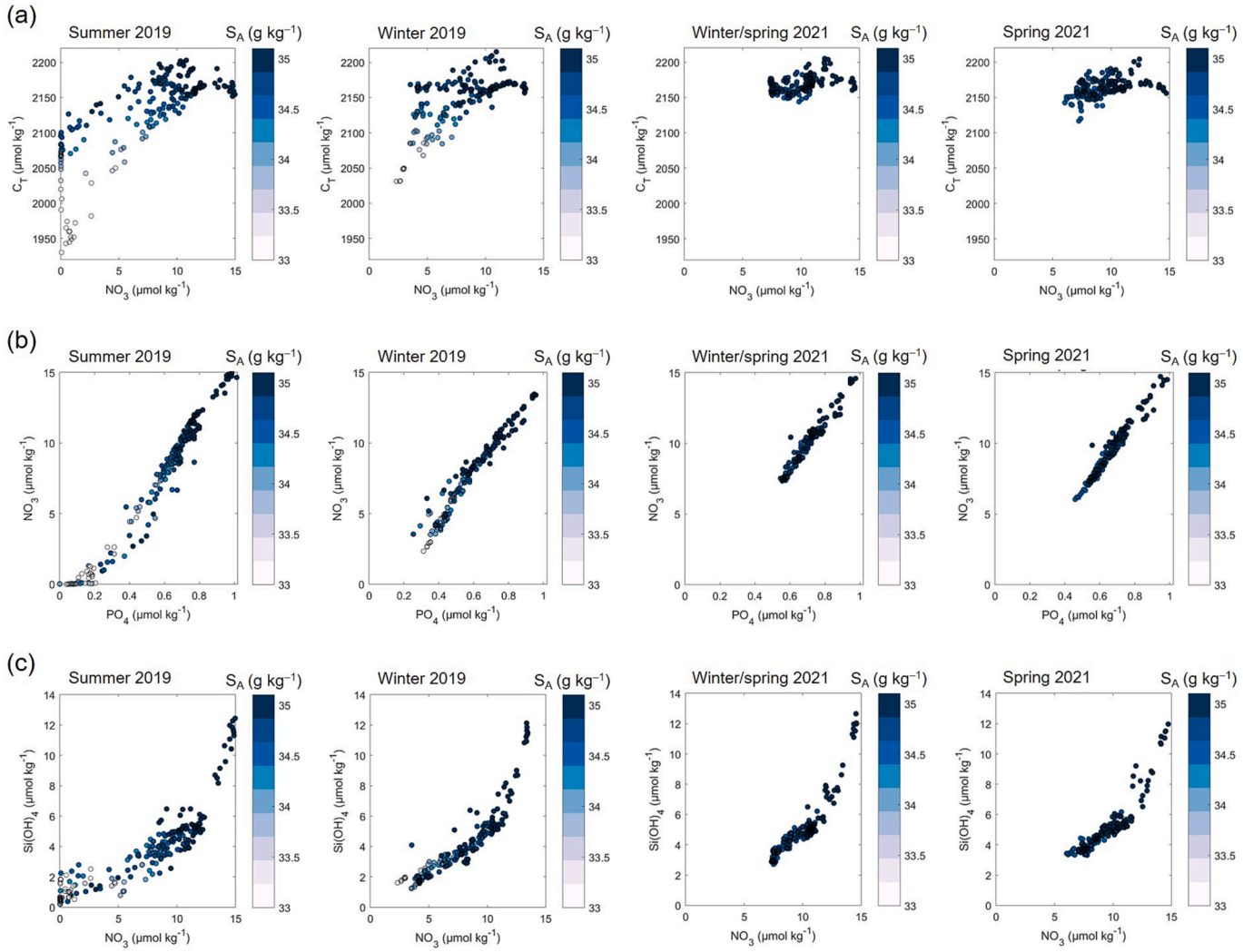

Fig. 8. Relationships between (a) C_T (μmol kg^{-1}) and NO_3 (μmol kg^{-1}) C:N, (b) NO_3 (μmol kg^{-1}) and PO_4 (μmol kg^{-1}) C:P, and (c) $Si(OH)_4$ (μmol kg^{-1}) and NO_3 (μmol kg^{-1}) Si:N, during summer (August 2019), winter (December 2019), winter/spring (March 2021) and spring (April-May 2021). Data are coloured by salinity (S_A; g kg^{-1}).

CBSDW (summer to winter 2019) to relatively warm wPW (winter/spring to spring 2021). The changes in water mass composition overlying the shelf impacted the carbonate system, particularly C_T, and showed that interannual variability was stronger than seasonal variability (Table 2). Across the shelf slope (P6), year-to-year variability was strong in the surface layer with higher sea-ice cover throughout 2019 and early 2020, shifting to less sea ice and warmer waters in the summer seasons of 2020 and 2021. A more regular seasonal pattern dominated the variability in deeper waters (Van Engeland et al., 2023). Therefore, the interannual variability introduced as a result of the sampling gap between 2019 and 2021 is likely to exert a greater impact on the perceived seasonality for waters most influenced by ice-ocean interactions, i.e. the surface layer and water column of the marginal ice zone (north of P2) across the Barents Sea shelf and slope.

To assess the impact of these different temporal scales on the seasonal dynamics, the biogeochemical conditions in the surface layer and at ~ 120 m depth of the northwestern Barents Sea (77–81 °N, 34 °E; from P2 to P5) were evaluated relative to a 5-year average (Table S1) (Jones et al., 2020; Jones et al., 2019; Jones et al., 2022c; Skjelvan et al., 2021) during consecutive summer seasons from 2018 to 2022 (one year either side of the study period). The summer season represented the greatest changes in total change in C_T and A_T (Fig. 10) and therefore can provide a good assessment of interannual variability in the upper water column and concurrent impacts on ΔC_T and ΔA_T that yield uncertainties in single-year estimates of ΔC_T and ΔA_T. Relative to the 5-year average ΔC_T ($\Delta C_{T\ ave}$; average surface – average 120 m), the difference in average ΔC_T in 2019 was 8 μmol kg^{-1} and yielded an estimated error on the 2019 total ΔC_T of 9 % due to interannual variability. The corresponding difference in ΔA_T (relative to $\Delta A_{T\ ave}$) was 2 μmol kg^{-1} and gives an estimated error on the 2019 total ΔA_T of 4 % due to interannual variability. The ΔC_T and ΔA_T determined in summer 2019, and NCP estimates relative to winter/spring and spring 2021 (section 3.6), are conservative with respect to the 5-year average from this region and can be considered as largely representative with regards to interannual variability in the northwestern Barents Sea.

4. Discussion

4.1. Summer to winter transition

4.1.1. Sea-ice meltwater and primary production drive reductions in carbon and nutrients in summer

Seasonal changes in C_T, A_T and inorganic nutrients in the upper layer of the Barents Sea were strongly influenced by meltwater released during the seasonal retreat of the ice pack and biological uptake following the progression of the growing season. Greatest seasonal

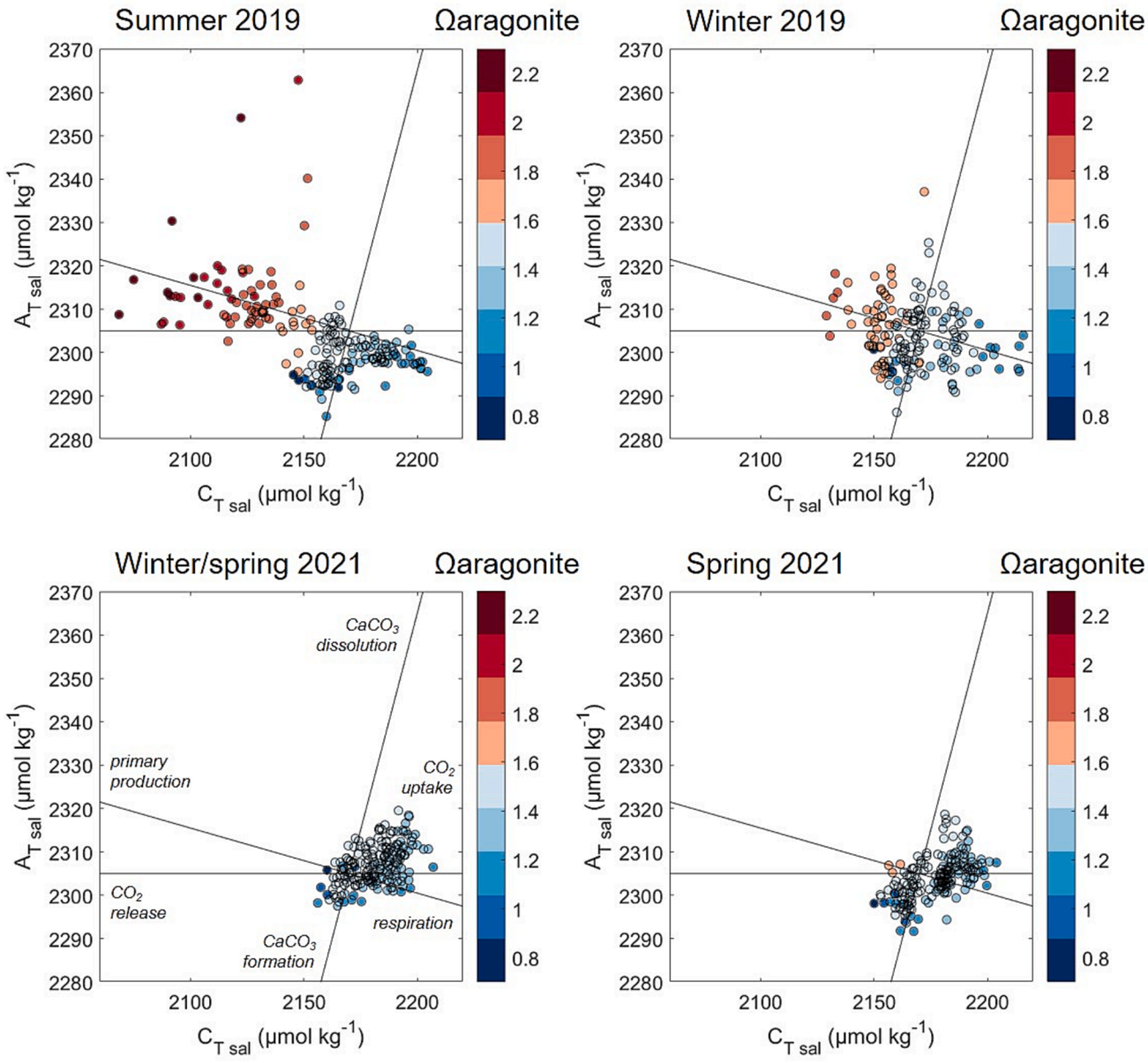

Fig. 9. Relationship between salinity-normalised A_T and C_T ($A_{T\ sal}$ and $C_{T\ sal}$; µmol kg^{-1}), following Friis et al. (2003), for (a) summer (August 2019), (b) winter (December 2019), (c) winter/spring (March 2021) and (d) spring (April-May 2021) coloured according to the saturation state of aragonite (Ωaragonite). Trend lines showing the theoretical slope for changes in $A_{T\ sal}$ and $C_{T\ sal}$ due to primary production/respiration, $CaCO_3$ dissolution/formation, and CO_2 uptake/release are shown from an arbitrary point in the $A_{T\ sal}$-$C_{T\ sal}$ space.

reductions in C_T and nutrients occurred in the relatively warm, fresh and ice-free waters with near-depleted NO_3 and low $Si(OH)_4$ in the surface layer (Fig. 11). Sea ice inflows from the Arctic Ocean and local sea ice formation and melt cycles contribute meltwater that forms the main freshwater source to the Barents Sea and wider Atlantic Water inflow region (Renner et al., 2018; Jones et al., 2021; Lundesgaard et al., 2021; Lundesgaard et al., 2022). Lowest C_T and A_T in the fresher Polar Water yielded largest changes in C_T and A_T in the upper 120 m with ΔC_T of − 13.1 mol m^{-2} (232 µmol kg^{-1}) and ΔA_T of − 8.5 mol m^{-2} (150 µmol kg^{-1}) driven by meltwater inputs that accounted for 55 % and 81 % of the summer ΔC_T and ΔC_T, respectively. The resultant elevated A_T:C_T and Ωaragonite in surface waters (Fig. 11g − h) were strongly driven by biological C_T uptake in the ice-free and meltwater-stabilised water column, which slightly counteracted effects of A_T dilution, resulting in biologically-driven increases in Ωaragonite and a buffer against acidification in summer surface waters.

In the wake of the retreating sea ice, meltwater inputs created a shallow meltwater lens that strengthens stratification in the surface layer (Leu et al., 2011; Koenig et al., this issue b). Surface waters were exposed increased light levels with a longer productive period and likely represented later-stage bloom conditions (in August) with contributions from regenerated production (Randelhoff et al., 2018; Henley et al., 2020). Increased biological uptake of C_T and nutrients was the major driver with seasonal maxima in $\Delta C_{T\ bio}$ of − 4.3 mol m^{-2} ($\Delta A_{T\ bio}$ of 0.7 mol m^{-2}) in Atlantic-regimes south of the Polar Front. Surface waters were substantially undersaturated in CO_2 relative to the atmosphere and with $\Delta C_{T\ flux}$ of 0.3–0.9 mol m^{-2} the region was a strong sink for atmospheric CO_2, which was also shown for the wider Barents Sea region in summer (Ericson et al., 2023).

Higher C:N uptake ratios (>10) in summer were indicative of ongoing C_T uptake under low NO_3 conditions in meltwater-influenced surface waters. The cycling of C_T, NO_3 and PO_4 became un-coupled

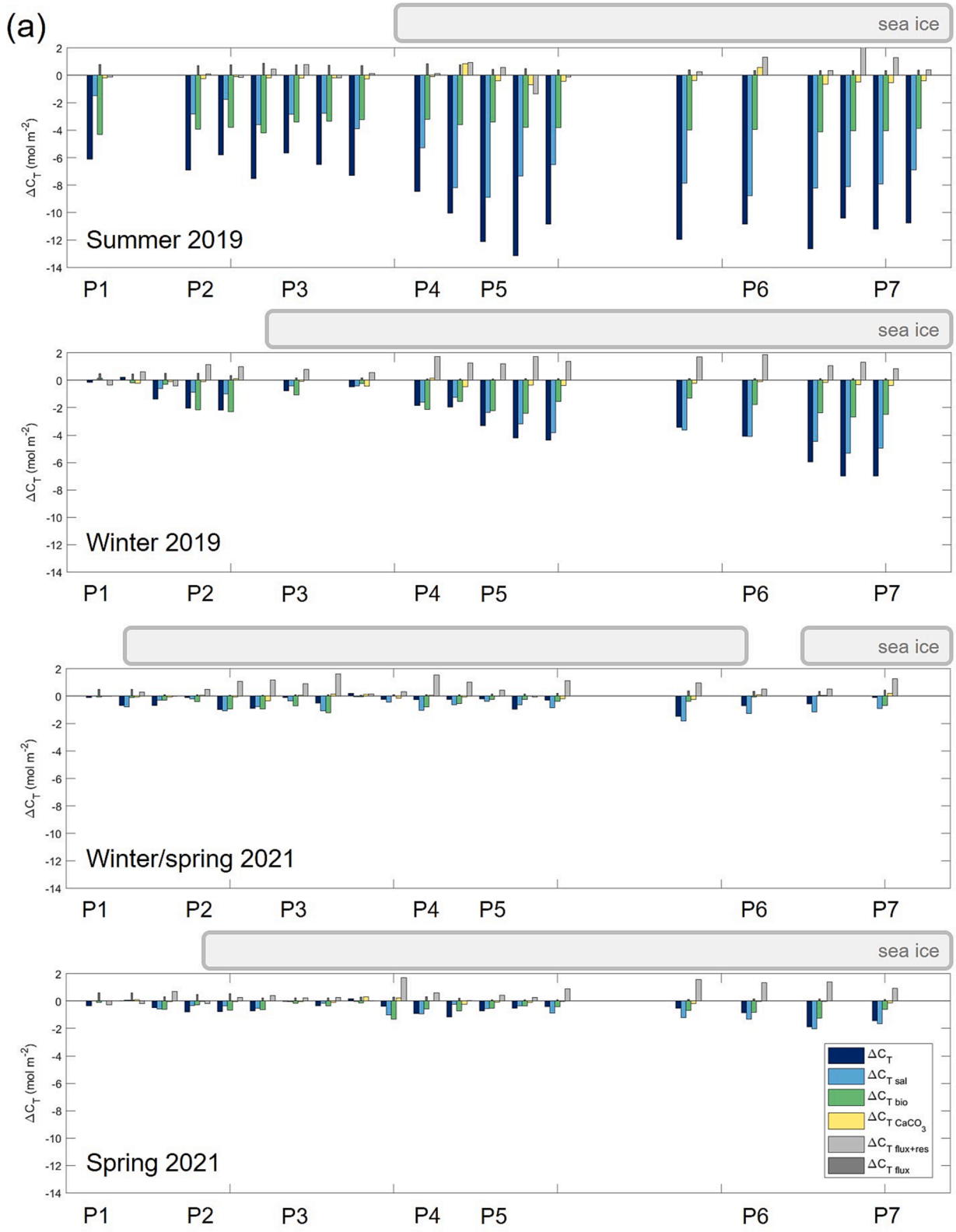

Fig. 10. Seasonal drivers of changes in (a) C_T (ΔC_T; mol m^{-2}) and (b) A_T (ΔA_T; mol m^{-2}) in the upper ocean (surface to 120 m) during summer (August 2019), winter (December 2019), winter/spring (March 2021) and spring (April-May 2021). Total change (ΔC_T, ΔA_T mol m^{-2}; dark blue bars) is partitioned into different processes of salinity changes ($\Delta C_{T\ sal}$, $\Delta A_{T\ sal}$; mol m^{-2}; light blue bars), primary production/respiration ($\Delta C_{T\ bio}$, $\Delta A_{T\ bio}$; mol m^{-2}; green bars), $CaCO_3$ formation/dissolution ($\Delta C_{T\ CaCO3}$, $\Delta A_{T\ CaCO3}$; mol m^{-2}; yellow bars), CO_2 fluxes and residual changes ($\Delta C_{T\ flux+res}$; mol m^{-2}; light grey bars) and air-sea CO_2 fluxes in the upper 10 m ($\Delta C_{T\ flux}$; mol m^{-2}; dark grey lines). Positive ΔC_T and ΔA_T indicate an increase in C_T and A_T, respectively, in the surface layer relative to 120 m depth; negative ΔC_T and ΔA_T indicate a decrease in C_T and A_T, respectively, in the surface layer relative to 120 m depth. Seasonal sea-ice cover is indicated by horizontal grey bars. (For interpretation of the references to colour in this figure legend, the reader is referred to the web version of this article.)

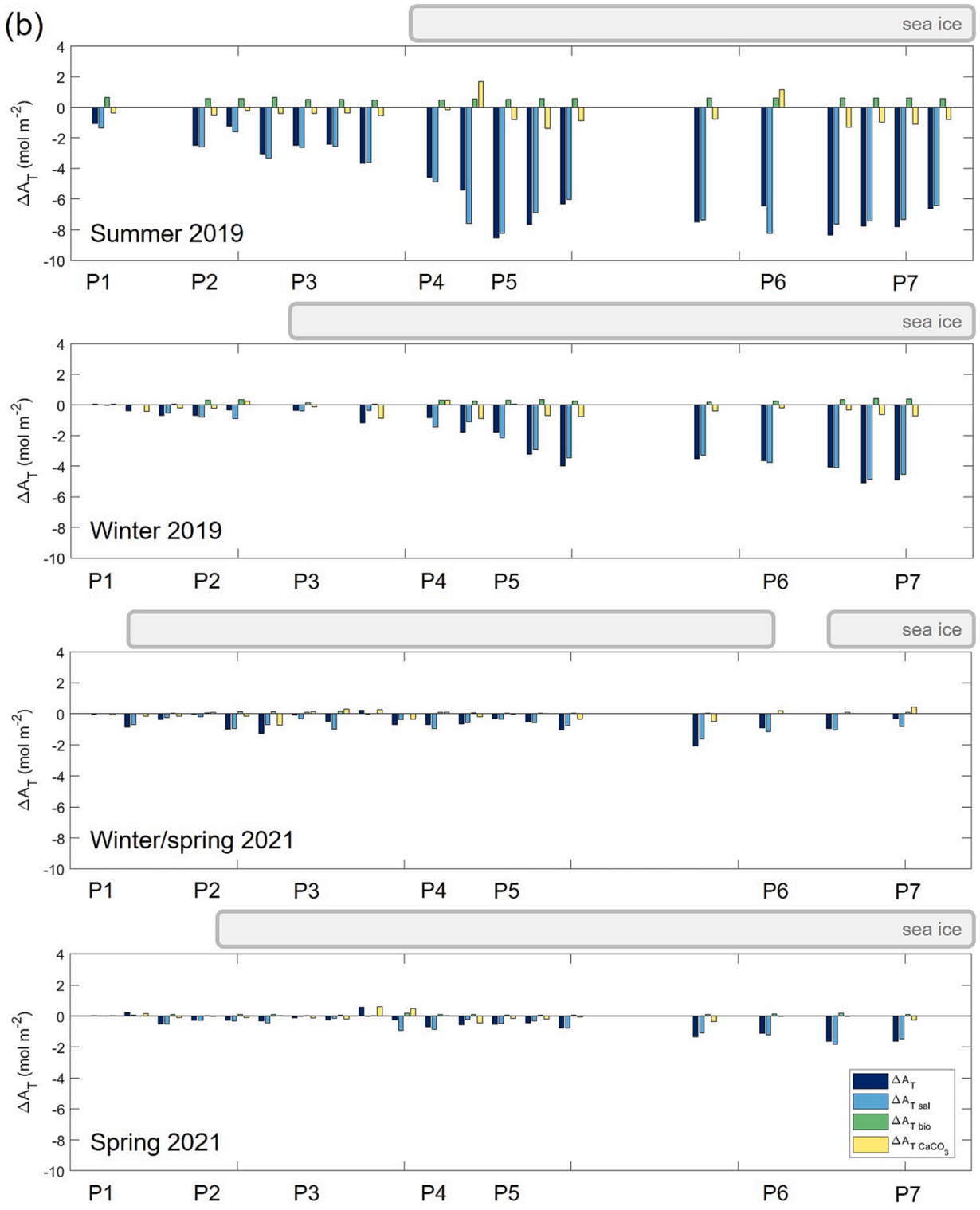

Fig. 10. (*continued*).

resulting in overconsumption of C_T at depleted NO_3 concentrations following the growing season. This occurred typically in open waters during the progression of summer with a likelihood of subsurface chlorophyll *a* maxima appearing as surface nutrients get depleted (Koenig et al., this issue b). High C:N uptake ratios and overconsumption of C_T relative to NO_3 has also been reported for the summer in the Atlantic Water inflow (Randelhoff et al., 2018), across the northern Svalbard shelf (Jones et al., 2021) and in Svalbard fjords (Ericson et al., 2019). Surface water C_T can also be affected by ice-algal production (Leu et al., 2011), which may contribute to production and C_T uptake signals in the pelagic blooms in the MIZ. Concurrent lower Si:N uptake ratios (~0.5) reflected $Si(OH)_4$ uptake that followed the species succession from spring to late summer. Concentrations of $Si(OH)_4$ were near or at depletion as a result of $Si(OH)_4$ uptake in diatom blooms following depletion of NO_3 in the surface layer due to earlier uptake by non-siliceous species, such as the haptophyte *Phaeocystis pouchetii* with (Reigstad et al., 2002; Assmy et al., 2017; Henley et al., 2020).

The northward decrease in NCP_{sum} from highest seasonal values of

Table 4
Net community production (NCP; mol C m^{-2}) estimated from changes in salinity-normalised nitrate concentrations ($\Delta NO_{3\ sal}$; μmol kg^{-2}) from winter/spring (March 2021) to spring (April-May 2021) NCP_{spr}, and from winter/spring (March 2021) to summer (August 2019) NCP_{sum}. $\Delta NO_{3\ sal}$ was integrated in the upper 50 m and converted to carbon using C:N stoichiometric ratio 106:16 (Redfield et al., 1963).

Station	Regime/ location	NCP_{spr} (mol C m^{-2})	NCP_{sum} (mol C m^{-2})
		March to April-May	*March to August*
P1	Atlantic Water inflow/ south of Polar Front	0.1	1.3
P2	Arctic/ Barents Sea shelf	0.0	1.0
P3	Arctic/ Barents Sea shelf	0.0	0.8
P4	Arctic/ Barents Sea shelf	0.2	0.9
P5	Arctic/ Barents Sea shelf	0.1	0.6
P6	Barents Sea shelf slope/ Atlantic Water inflow	0.3	0.6
P7	Nansen Basin	0.0	0.4
average		*0.1 ± 0.1*	*0.8 ± 0.3*

1.3 mol C m^{-2} (14 g C m^{-2}) in the Atlantic regime at P1 to 0.4 mol C m^{-2} (5 g C m^{-2}) in the Nansen Basin at P7 followed the seasonal retreat of the sea ice and the comparative increased primary production in ice-free waters. Using the same nitrate-derived carbon uptake approach, spring NCP (January to May) of 26 g C m^{-2} and summer NCP (January to August) of 36 g C m^{-2} were determined along the Atlantic Water inflow in eastern Fram Strait (Chierici et al., 2019), which are close to the range 28–32 g C m^{-2} estimated for annual export production in the Barents Sea (Fransson et al., 2001). These estimates are approximately 50 % larger than the highest NCP_{sum} of 14 g C m^{-2} in the Atlantic Water inflow from this study, which is likely due time period of seasonal biological production (March taken as wintertime pre-bloom conditions versus January as in Chierici et al., 2019) and the more northerly location with seasonal sea-ice cover delaying primary production. Furthermore, the NCP_{sum} estimates determined from changes in NO_3, referred to as new production, do not consider biological production using other inorganic nitrogen sources (Chierici et al., 2019) and reveal the range of NCP estimates for the Arctic Ocean region depending on the approach used and the temporal and spatial scales selected. The NCP_{spr} and NCP_{sum} values corresponded to daily rate of change since winter/spring (March) of approximately 20 ± 27 mg C m^{-2} d^{-1} by spring (April-May) and 64 ± 24 mg C m^{-2} d^{-1} by summer (August) in the upper 50 m. The NCP_{spr} and NCP_{sum} estimates of organic matter production from biological carbon (NO_3) uptake align with the general trend of organic carbon export rates in the upper 30–200 m, with high and spatially variable fluxes (178 ± 202 mg C m^{-2} d^{-1}) from diatom blooms in May and less variable fluxes (159 ± 79 mg C m^{-2} d^{-1}) with greater contribution from small flagellates in August (Bodur et al., 2023).

Decreased A_T up to 1.4 mol m^{-2} in the upper layer ascribed to $CaCO_3$ processes suggested formation of $CaCO_3$, which could result from biotic $CaCO_3$ formation by calcifying organisms or precipitation of ikaite from sea ice (Fransson et al., 2013). The changes in A_T indicated that $CaCO_3$ processes were seasonally important in decreasing A_T (accounting for 10 % of ΔA_T) in the surface layer in summer. The formation of $CaCO_3$ shells and skeletons in waters of the Barents Sea occursby phytoplankton and zooplankton both locallyand/or signals of $CaCO_3$ production advected in the Atlantic Water inflow (Chierici et al., 2019; Oziel et al., 2020; Jones et al., 2021). The calcifying phytoplankton Emiliania huxleyi has calcitic shells (coccoliths) and has expanded its geographic range northwards in the Atlantic Water inflow and has been found to maintain growth under nutrient limited conditions in the Barents Sea (Hegseth and Sundfjord, 2008; Oziel et al., 2020). Additionally, the calcifying zooplankton pteropods (aragonitic shells) and foraminifera and have been found with highest seasonal abundances in summer (Zamelczyk et al., 2021; Anglada-Ortiz et al., 2023). Pteropods and foraminifera are key producers of $CaCO_3$, contributing to A_T and C_T changes through calcification or $CaCO_3$ dissolution, and seasonal carbon export and fluxes in the Barents Sea (Anglada-Ortiz et al., 2023). Another possible mechanism of reduced A_T from $CaCO_3$ processes in seasonally-ice covered waters is from ikaite formation in sea ice (Rysgaard et al., 2007). Meltwater release may transfer a signal of ikaite formation to surrounding surface waters (Rysgaard et al., 2007; Fransson et al., 2013; Chierici et al., 2019).

4.1.2. *Winter surface waters imprinted by meltwater dilution and biological processes*

Increased remineralisation of organic matter and mixing from late summer to early winter shifted the conditions in the Barents Sea from substantial biological carbon uptake and a strong atmospheric CO_2 sink towards areas of net increases in C_T (ΔC_T up to 0.2 mol m^{-2}) in the upper layer. Atmospheric cooling of surface waters increased the extent of Polar Water and the pack ice expanded southward during the transition to winter. The southern part of the region was ice-free (Fig. 2) for a longer period and showed smaller seasonal changes in C_T and A_T from vertical mixing into subsurface Atlantic Water (and Atlantic-influenced waters). The biologically-driven decreases in C_T and NO_3 at the end of the growing season had been eroded and wind-driven mixing dispersed the lower C_T and NO_3 signature and lowered C:N and N:P ratios deeper into the water column. Replenishment of C_T and NO_3 occurred in the upper layers (Fig. 5 − 6) from subsurface waters alongside inputs from organic matter remineralisation. This was most notable at southern locations, with higher C_T (and A_T) in the surface layer south of the ice edge that contributed to variability in NO_3 and $Si(OH)_4$ with lower concentrations below 100 m depth (Fig. 6). Negating effects of inputs of A_T from intrusions of Atlantic-influenced waters, these processes reduced the A_T:C_T ratio and Ωaragonite in the upper layer. Since the preceding summer, nutrient-recycling and remineralisation (Randelhoff et al., 2018; Henley et al., 2020) and advective fluxes from Atlantic Water (Koenig et al, this issue a) could re-supply NO_3 to alleviate any nutrient limitation in the presence of late-stage phytoplankton communities (Randelhoff et al., 2015; Slagstad et al., 2015; Tremblay et al., 2015) to prolong C_T uptake through the autumn and contribute to a wintertime biological-uptake signal with $\Delta C_{T\ bio}$ around − 2.7 mol m^{-2} in the Nansen Basin.

The fresher Polar Water surface layer in Arctic regime in the Nansen Basin reflected effects of relative freshening in the upper layers, whilst vertical mixing increased the salinity, C_T and A_T in the water column to counteract the effects of dilution south of the winter ice edge. Decreases in A_T up to 0.9 mol m^{-2} around the ice edge could be attributed to $CaCO_3$ precipitation, which follows the lowered-A_T signal of biotic calcification and/or abiotic ikaite formation from the summer. A decoupling between C_T and A_T variability was evident in the water column as C_T had greater increases than A_T (and salinity), suggesting different driving processes or sources of C_T and A_T during the summer to winter transition. The relative increase in $C_{T\ sal}$ at near-constant $A_{T\ sal}$ indicated that atmospheric CO_2 uptake in the cooling surface water had a key role in increasing C_T since the summer (Fig. 9). The uptake of atmospheric CO_2 that was driven by primary production was slightly counteracted by mixing with subsurface waters and late-stage blooms, with an average ice-scaled $\Delta C_{T\ flux}$ of 0.2 mol m^{-2} dampened from an average summertime $\Delta C_{T\ flux}$ of 0.6 mol m^{-2} (Fig. S3) across the region. Concomitant thermodynamic reductions in surface water Ωaragonite also occur during winter cooling, alongside increased C_T from CO_2 inputs (Fig. 11), as the solubility of aragonite increases with decreasing temperature (Mucci, 1983).

4.2. *Winter to spring transition*

4.2.1. *Mixing, organic matter remineralisation and sea-ice processes enrich carbon and nutrients below the ice pack*

Vertical mixing, remineralisation of organic matter and CO_2 fluxes

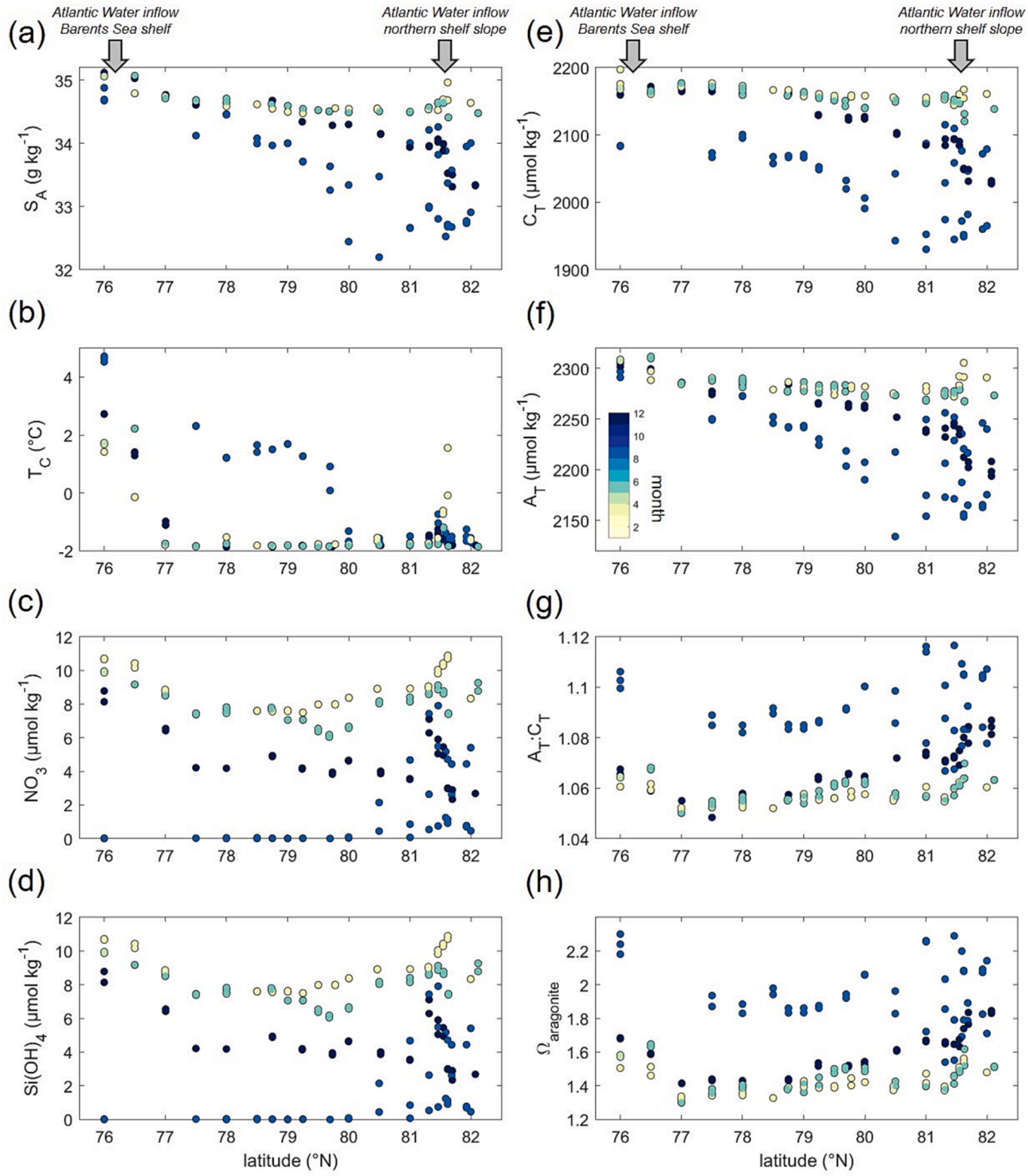

Fig. 11. Surface water (<15 m) (a) S_A (g kg^{-1}), (b) T_C (°C), (c) NO_3 (µmol kg^{-1}), (d) $Si(OH)_4$ (µmol kg^{-1}), (e) C_T (µmol kg^{-1}), (f) A_T (µmol kg^{-1}), (g) the A_T:C_T ratio and (h) Ωaragonite along the transect. Data are colour coded by month of sampling with the legend in (f). The general location of the Atlantic Water inflow in the southern Barents Sea shelf and northern shelf slope is marked by grey arrows.

enriched the water column with C_T, A_T and nutrients beneath the sea ice by winter/spring (March). This resulted in highest concentrations of C_T, A_T and NO_3 in the Polar Water layer and highest C_T, NO_3 and $Si(OH)_4$ in Atlantic-influenced water masses across the region out of all seasons. Mixing of Atlantic Water and replenishment of C_T and NO_3 was particularly evident along the inflow pathways (Fig. 5). The well mixed water column had low ΔC_T and ΔA_T with lowest variability and small range out of all the seasons. The water column was more homogenous and mixing with subsurface Atlantic Water (salinity-driven changes) was a key driver accounting for 39 % and 85 % of ΔC_T and ΔA_T,

respectively. Small changes as a result of meltwater inputs ($\Delta C_{T\ sal}$ and $\Delta A_{T\ sal}$) occurred with localised erosion of the sea-ice cover through shoaling Atlantic-derived water masses over the slope and in the Nansen Basin. Deep mixed layers and low chlorophyll *a* concentrations (Koenig et al., this issue b) reflected the low biological activity and resulted in small contributions from biological and $CaCO_3$ processes. This coincided with lowest seasonal abundances of the calcifying zooplankton foraminifera and pteropods that were found in winter/spring (Anglada-Ortiz et al., 2023).

The cooled surface waters and increased $C_{T\ sal}$ indicted that atmospheric CO_2 uptake was also driving changes in C_T prior to substantial sea-ice cover, with C_T increases in the surface layer (ice-scaled $\Delta C_{T\ flux}$) of 0.5 mol m^{-2} that contributed to the greatest seasonal change due to $\Delta C_{T\ flux+res}$ (37 % of ΔC_T) with average $\Delta C_{T\ flux+res}$ values of 0.7 mol m^{-2}. This likely included inputs of CO_2 from the rejection of CO_2-rich brines from forming sea ice where ikaite formation has taken place and would partition A_T in the sea ice and enrich C_T in the brine (Rysgaard et al., 2007). These processes enabled C_T to become enriched in the upper layers and drive thermodynamic reductions in Ωaragonite and lowering the A_T:C_T ratio in the water column. Relative to the other seasons, lowest C:N and highest N:P ratios in winter/spring resulted from organic matter remineralisation and mixing with Atlantic Water that enriched the water column with NO_3 relative to C_T. Lower C:N and higher N:P have been previously reported for Atlantic-influenced waters in the Barents Sea region (Frigstad et al., 2014; Jones et al., 2021). Concurrent higher Si:N ratios resulted from dissolution of diatom frustules and/or mixing with $Si(OH)_4$-rich Intermediate Water over the shelf. Warm Polar Water occupied the deep layer of the shelf, rather than CBSDW that was found in summer and winter 2019 (discussed further in section 4.3) and represented a nutrient (and A_T) source to overlying Polar Water if vertical mixing processes occurred. This showed interannual variability in ice-ocean processes influencing water mass structure in the deeper water column across the shelf.

4.2.2. Spring blooms, sea-ice melt and seasonal reductions in carbon and nutrients

The general northward retreat of the sea ice and degraded sea ice along the Atlantic Water inflow (Fig. 2) exposed the nutrient-rich surface layer to increasing light levels and meltwater stabilisation in spring (April-May). Smaller seasonal changes in ΔC_T of − 1.9 mol m^{-2} and ΔA_T of − 1.7 mol m^{-2} reflected conditions of the well-mixed column with relatively little change since early spring (March). The high C_T and A_T content in the upper and Atlantic-influenced layers was pre-conditioned by vertical mixing, organic matter remineralisation, CO_2 fluxes and inputs from CO_2-rich brines since the winter. The variability in C_T and A_T closely followed that of the early spring with values similar to those at the end of winter as a starting point for the changes in concentration that followed.

Excess A_T in the surface layer relative to subsurface waters indicated a surface source of A_T ($\Delta A_{T\ CaCO3}$ up to 0.6 mol m^{-2}; only accounting for 5 % of average ΔA_T). Sources of $CaCO_3$ include shells and skeletons of phytoplankton and zooplankton in the water column (Anglada-Ortiz et al., 2023) or advection in the Atlantic Water inflow (Chierici et al., 2019; Oziel et al., 2020). Another possible source of A_T and C_T from $CaCO_3$ in seasonally-ice covered waters is from the dissolution of ikaite released from sea ice (Rysgaard et al., 2007) during early ice melt in spring. Potential minor contributions of A_T could also result from glacial meltwater originating from Svalbard (Ericson et al., 2019), river runoff from Svalbard and Arctic rivers (Cooper et al., 2008) and precipitation, which is expected to be insignificant compared to contributions from sea-ice (local and advected) meltwater (Koenig et al., this issue b).

Nutrient and C_T concentrations in surface waters showed a slight northward decrease relative to earlier spring (March) concentrations indicating uptake (prior to significant dilution) in the Polar Water over the central shelf. Pelagic phytoplankton in Arctic waters typically start to bloom following significant melt and retreat of the seasonal ice pack to increase light availability (Reigstad et al., 2002; Leu et al., 2011). The onset of seasonal sea-ice melt in spring and favourable light levels was sufficient to promote phytoplankton production and an early spring bloom despite deep mixed layers in ice-covered waters (Koenig et al., this issue b). Additionally, nutrients, phytoplankton and upstream blooms could be advected along the Atlantic Water inflow to enhance the spring nutrient and C_T uptake signal despite the presence of seasonal sea ice (Assmy et al., 2017; Henley et al., 2020). This resulted in a reduction in surface layer concentrations of NO_3, C_T and A_T compared with winter/spring values. Dilution in the upper layer lowered C_T and A_T, particularly over the northern shelf and Nansen Basin. Increased C:N ratios and decreased N:P ratios traced reductions in C_T following uptake of NO_3, consistent with nutrient and carbon stoichiometry of biological uptake. Reductions in C_T in the upper layer ($\Delta C_{T\ bio}$) up to − 1.3 mol m^{-2} increased during the seasonal transition, enhancing the A_T:C_T ratio and biologically-driven increases in Ωaragonite. Springtime NCP estimates were more spatially variable than the NCP estimates in summer with the highest value of 0.3 mol C m^{-2} (4 g C m^{-2}) in the Atlantic Water inflow across the northern shelf slope. The NCP_{spr} was about 25 % of the maximum summer NCP and was located in partially ice-covered waters and may have contributions from ice algae production (Leu et al., 2011). Higher NCP of 16 ± 6 g C m^{-2} and 15 ± 5 g C m^{-2} was previously derived from biological carbon uptake and equivalent nitrate-derived carbon consumption, respectively, in the upper 50 m further west in the Nansen Basin during the spring bloom period in May to June (Assmy et al., 2017; Fransson et al., 2017). The almost four-fold higher values in the west in the Nansen Basin likely result from later stage spring bloom and more nitrate uptake.

4.3. Acidification of intermediate and deep waters in the Barents sea and Nansen Basin

In summer and winter 2019, localised deepening of the isolines over the shelf indicated the presence of cold ($T_C \leq -1.1$ °C) and dense CBSDW between 78.7 and 80°N and cool Intermediate Water at 77.5 and 78.7°N (Fig. 12). Both water masses occupied a greater area in summer and persisted into winter (Fig. 4). From winter to spring 2021, no Intermediate Water or CBSDW was found over the shelf, instead warm Polar Water occupied this depth range (about 100 –300 m) below a water column dominated by Polar Water. The CBSDW showed slightly reduced NO_3 and similar $Si(OH)_4$ and A_T (~2300 μmol kg^{-1}) content relative to the warm Polar Water that occupied this depth and location from winter to spring. A notable difference was elevated C_T ~ 2190 μmol kg^{-1} with Ωaragonite ~ 1.2 and lowest A_T:C_T ratio of 1.05 (Fig. 12) and the least buffered waters in the Barents Sea. The similar A_T content could be considered as a semi-conservative tracer to suggest that any meltwater dilution was largely counteracted by advected supply of high A_T water. Therefore, the elevated C_T showed that other (non-biological, non-mixing/advective) processes contributed to enrichment of C_T relative to NO_3 and A_T in the CBSDW.

Taking the hydrographic conditions to represent both seasonal and interannual variability (2019 vs. 2021; as also reported in Van Engeland et al. (2023)), the changes in water mass structure that followed indicated some key processes influencing carbonate chemistry (Table S1) (Jones et al., 2020; Jones et al., 2019; Jones et al., 2022c; Skjelvan et al., 2021), nutrient cycling and acidification state over the shelf. The 2018/19 winter period had strong surface cooling, sea-ice formation and deep convection, resulting in a wider expanse of the ice pack and the production of cold, saline Intermediate Water and CBDSW (Lundesgaard et al., 2022; Van Engeland et al., 2023). The Intermediate Water and CBDSW present over the shelf in summer and early winter 2019 were remnants of the cooling, deep convection and enhanced sea-ice formation of the preceding 2018/19 winter period. In 2019, sea-ice inflows into the Barents Sea covered a substantially wider areal extent and contributed more freshwater to the region (Lundesgaard et al., 2022; Renner et al., this issue). The elevated C_T and salinity of the CBSDW

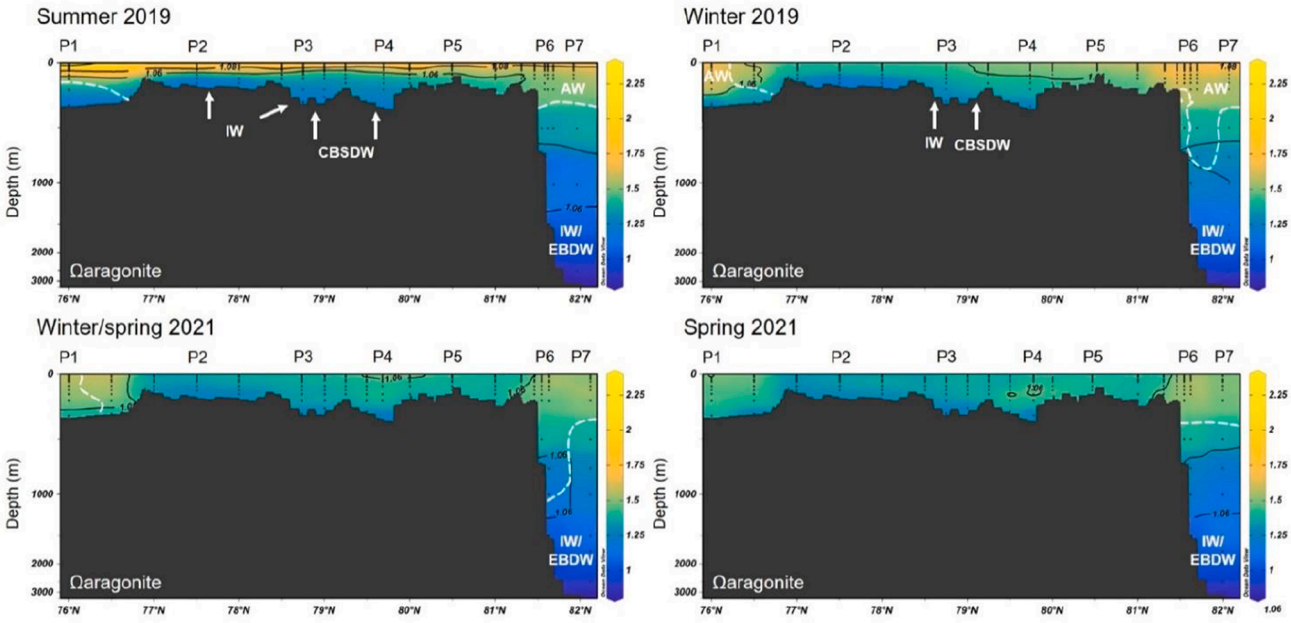

Fig. 12. Transect section plots of Ωaragonite during summer (August 2019), winter (December 2019), winter/spring (March 2021) and spring (April-May 2021). Contours are shown for the A_T:C_T ratio (thin black lines) and absolute salinity of 35.06 g kg^{-1} (dashed white line) that distinguishes modified Atlantic Water and Atlantic Water. Water masses Atlantic Water (AW), Cold Barents Sea Dense Water (CBSDW), Intermediate Water (IW) and Eurasian Basin Deep Water (IW/EBDW) are labelled. The locations of the process (P) stations are labelled. Ocean Data View was used for data visualisation (Schlitzer, 2022).

reflected the impact of deep wintertime convection and ice-ocean processes where CO_2-rich brines expelled from forming sea ice enriched subsurface water with C_T under the winter sea ice (Fransson et al., 2013). Following the period of cooling and convection, the southward expanding ice pack capped the water column to reduce vertical mixing and warm Polar Water was found encroaching the central shelf from the Atlantic Water inflow over the northern shelf. The acidified CBSDW layer became largely diminished showing seasonal variability.

In contrast, the 2020/21 winter period had less surface cooling and reduced convection, limiting production of cold and saline subsurface waters over the shelf (Van Engeland et al., 2023). Instead, warm Polar Water was found overlying the shelf, from recirculated Atlantic Water that enters the region from the northern inflow and is subsequently modified by cooling and freshening by mixing with Arctic waters (Renner et al., 2018). Modifications of water masses are likely reflected in the A_T, C_T and nutrient content through a balance of organic matter remineralisation and silicic acid and carbonate dissolution versus dilution processes. The Barents Sea and Atlantic Water inflow shelves experiences significant interannual variability in sea ice (Renner et al., this issue) and winters of less sea ice imports, reduced cooling and convection can therefore lead to increased presence of Atlantic-influenced waters (Van Engeland et al., 2023) that represent an additional source of nutrients and A_T to pre-condition the water column over the central shelf for the following growing and meltwater seasons.

In the Nansen Basin, IW/EBDW occupied the intermediate and deep layers (below 1000 m deep) in all seasons (Fig. 4). Intermediate Water was relatively nutrient rich, especially with respect to $Si(OH)_4$, with slightly lower A_T (~2302 μmol kg^{-1}) and slightly higher C_T (~2169 μmol kg^{-1}) compared with Atlantic Water. The average water mass characteristics showed some variability in C_T, A_T and nutrients, and a low A_T:C_T ratio ~ 1.06. Values of Ωaragonite were 0.76–1.22 at 1000–3650 m and the saturation horizon for aragonite (Ωaragonite = 1) was located at 1500–2000 m depth in the Nansen Basin (Fig. 12). Reductions in Ωaragonite of 0.05–0.14 during 1994–2011 (Ericson et al., 2014) and 0.04–0.06 during 1996–2015 (Ulfsbo et al., 2018) have been found in Atlantic Water and Intermediate Water layers (~100–1500 m) in the Arctic Ocean. For initial Ωaragonite values of 1.2–1.4 (Ericson et al., 2014), the corresponding rate of change in Ωaragonite was therefore − 0.002 and − 0.003 per year in the Intermediate Water layer. In the Nansen Basin at ~ 82 °N, Jones et al. (2021) reported Ωaragonite of 1.13 ± 0.02 in Intermediate Water at 1500 m in 2015 and this study found Ωaragonite of 1.11 ± 0.03 at 1500 m (at P7, ~82 °N) for the years 2019 to 2021. The Atlantic Water inflow into the Arctic Ocean transports anthropogenic CO_2, from atmospheric uptake in the Atlantic Ocean, and inputs from organic matter remineralisation into Intermediate Waters of the Nansen Basin. The reported decline in Ωaragonite Intermediate Waters results from the accumulation of C_T at intermediate depths that are isolated from the surface ocean, therefore limiting connectivity and ventilation in the Arctic Ocean (Ericson et al., 2014; Ulfsbo et al., 2018). Following initial Ωaragonite conditions from Ericson et al. (2014), it is estimated that Ωaragonite in Intermediate Water in the Nansen Basin has decreased by ~ 0.07 in 20 years (Jones et al., 2021) and ~ 0.09 in about 25 years (this study). This corresponds to a change in Ωaragonite of − 0.003 and − 0.004 per year, respectively, and indicates that the rate of decrease of Ωaragonite (enhanced risk of acidification) has slightly increased across the different study periods since 1994. Therefore, the shallower limit (~1500 m) of Intermediate Water in the Nansen Basin could experience acidification with undersaturation of aragonite in the next 50–100 years.

4.4. Atlantic Water connectivity alleviates surface water acidification along the inflow pathways in the Barents sea

. A more Atlantic-like regime along the inflow pathways south of the Polar Front and in the upper ~ 500 m across the slope and into the Nansen Basin shaped the biogeochemical characteristics and drivers of C_T and A_T in the upper water column (Fig. 4). Both regions of Atlantic Water inflow had highest A_T:C_T ratios and Ωaragonite in surface waters in summer and elevated Ωaragonite in the upper layer in the other seasons relative to other waters across the Barents Sea shelf (Fig. 12). The Atlantic Water inflow south of the Polar Front generally displayed the lowest seasonality in inorganic carbon and nutrient cycling. Seasonally ice-free, wind-induced mixing maintained a more homogenous water mass structure during each season (Fig. 3) with small

changes in C_T and A_T in the upper water column relative to the rest of the Barents Sea shelf and Nansen Basin (Fig. 11). Primary production was the biggest driver of seasonal C_T change and increased NCP to a summer maximum of 1.3 mol C m^{-2} relative to the rest of the region with concurrent high standing stocks of chlorophyll *a* (Koenig et al., this issue b) and nutrient resupply (Koenig et al, this issue a) within a persistent Atlantic-like regime.

The Atlantic Water inflow over the northern shelf slope displayed strong seasonality in C_T and nutrients and some of the largest changes in C_T and A_T in the upper water column (through reduced C_T and A_T in the surface layer) relative to the rest of the Barents Sea. Seasonally covered in sea ice with varying conditions (Renner et al., this issue), reduced wind-driven mixing sustained a more stable water column typically capped with Polar Water. Shoaling of Atlantic-influenced waters into the surface layer over the slope and Nansen Basin likely contributed to degradation of the sea ice in March 2021 (Fig. 2). This region exhibits variable ice conditions (Renner et al., this issue) and is sometimes ice-free from winter to early spring due to Atlantic Water intruding the surface, with subsequent heat loss and melting of the seasonal sea ice (Onarheim et al., 2014; Duarte et al., 2020). Ice-free waters and subsequent wind-driven mixing can allow nutrients to enrich the upper layer (Randelhoff and Sundfjord, 2018), which was evident by increased temperature, salinity and NO_3 in the surface waters. This was accompanied by localised increases in A_T, elevated A_T:C_T ratio and higher Ωaragonite. In addition, springtime NCP was highest (0.3 mol C m^{-2}) relative to the rest of the region, fuelled by favourable light levels in patchy sea-ice cover and nutrient influx from below, in addition to advection of nutrients and phytoplankton along the inflow. Atlantic Water ventilation and connectivity along the northern shelf induced a transient Atlantic-like regime within the Arctic regime. The region is known to reflect signals from ice-ocean and biogeochemical processes that take place upstream in the inflow (Randelhoff et al., 2018; Renner et al., 2018; Lundesgaard et al., 2021) and shows that advective fluxes have an important influence on inorganic carbon and nutrient cycling and the state of ocean acidification downstream on the Barents Sea shelf and slope (Jones et al., 2021; Renner et al., this issue).

The Atlantic Water inflow pathways in the Barents Sea exhibited enhanced A_T from advection, $CaCO_3$ dissolution and biological production (increases in Ωaragonite). The concomitant increases in C_T (decreases in Ωaragonite) from the carbon-rich Atlantic Water likely resulted in transient offsets to the physical, geochemical and biological mechanisms driving increases in Ωaragonite. However, in the presence of active phytoplankton communities and favourable light levels, the resupply of NO_3 facilitates C_T uptake and yields net increases in Ωaragonite. These synergistic processes resulted in (i) generally elevated nutrients (except for depleted NO_3 in summer), C_T and A_T and low seasonality in the ice-free, mixed water column south of the Polar Front and (ii) increased nutrients, C_T and A_T and high seasonality in the ice-influenced water column over the shelf slope and Nansen Basin. Atlantic-derived A_T supplied to productive surface waters enhanced the buffering capacity (increased A_T and decreased C_T), resulting in seasonally and spatially elevated Ωaragonite as a mechanism to counteract ocean acidification in the Atlantic Water inflow regions of the Barents Sea.

5. Conclusion

Variability in inorganic carbon and nutrient cycling in the Barents Sea was strongly coupled to sea-ice cover and meltwater release, different water masses, biological production/remineralisation and $CaCO_3$ processes, which exerted seasonal controls on the state of ocean acidification (Ω) across the Atlantic and Arctic regimes. Seasonally elevated Ω (Ωaragonite up to 2.30) in the surface layer occurred along the Atlantic Water inflow pathways from connectivity to Atlantic-influenced waters that increased A_T alongside biological C_T uptake. Nitrate-derived NCP in the upper 50 m was enhanced in spring (0.3 mol C m^{-2}) and summer (1.3 mol C m^{-2}) in the Atlantic-like regimes.

In summer, C_T and A_T changes were driven by meltwater dilution (55 % of ΔC_T; 81 % of ΔA_T) and biological carbon uptake during primary production (37 % of ΔC_T). This resulted in enhanced surface water Ω south of the ice edge. Winter cooling, deep convection and sea-ice processes resulted in lower A_T and elevated C_T, driving low Ω (Ωaragonite 1.12–1.14) and risk of acidification in Arctic-like regimes over the shelf. From winter to early spring, C_T increases were explained by a combination of vertical mixing, remineralisation of organic matter, atmospheric CO_2 uptake and release of CO_2-rich sea ice brines. The water column was replenished with inorganic nutrients prior to the following growing season. The onset of the spring blooms and ice melt initiated the meltwater- and biologically-driven reductions in A_T and C_T and uptake of nitrate in surface waters. Formation and dissolution of biotic and abiotic $CaCO_3$ contributed to 5–13 % of ΔA_T. This is the first study investigating a full seasonal cycle of CO_2 fluxes in the marginal ice zone of the Barents Sea. Surface waters across Atlantic and Arctic regimes acted as a net annual sink of atmospheric CO_2. The intermediate and deep waters in the Nansen Basin revealed ongoing acidification trends from inflowing carbon-rich Atlantic-influenced waters. Understanding the seasonal dynamics and drivers of inorganic carbon and nutrient cycling in the Barents Sea is essential to understand the state of ocean acidification and determine the future impacts of Atlantification, which can have cascading consequences for the ecosystem along the Atlantic Water inflow and into the Arctic Ocean.

Funding

This work was funded by the Research Council of Norway through the project *The Nansen Legacy* (RCN 276730) and by the European Union's Horizon 2020 research and innovation programme under grant agreement number 820989, project COMFORT (Our common future ocean in the Earth system – quantifying coupled cycles of carbon, oxygen, and nutrients for determining and achieving safe operating spaces with respect to tipping points).

Declaration of Competing Interest

The authors declare that they have no known competing financial interests or personal relationships that could have appeared to influence the work reported in this paper.

Data availability

Data are reported in Chierici et al. (2021a), Chierici et al. (2021b), Gerland (2022), Jones et al. (2022a), Jones et al. (2022b), Ludvigsen (2022), Reigstad (2022) and Søreide (2022) and are available from the Norwegian Marine Data Centre.

Acknowledgments

The authors are most appreciative of the assistance provided by the Captain and crew of R/V *Kronprins Haakon*, cruise participants and cruise leaders (M. Reigstad and T. Gabrielsen; J. Søreide and R. Gradinger; S. Gerland and A. Wold; M. Ludvigsen and P. Assmy; M. Reigstad) for support during the Nansen Legacy cruises in 2019 (Q3 and Q4) and in 2021 (Q1 and Q2). Extended thanks to Griselda Anglada-Ortiz, Ylva Ericson, Katarzyna Zamelczyk, Claire Mourgues and Stephen Kohler for assistance in water sampling, analysis, scientific discussions and data quality assurance. This work was funded by the Research Council of Norway through the project *The Nansen Legacy* (RCN 276730) and by the European Union's Horizon 2020 research and innovation programme under grant agreement number 820989, project COMFORT (Our common future ocean in the Earth system – quantifying coupled cycles of carbon, oxygen, and nutrients for determining and achieving safe operating spaces with respect to tipping points). The authors

gratefully acknowledge the valuable comments from two anonymous reviewers that have improved the manuscript. The CTD and inorganic nutrient data are available from the Norwegian Marine Data Centre with references included in the text. The carbonate system data will be published upon acceptance of the manuscript. The authors gratefully acknowledge the valuable comments from two anonymous reviewers that have improved the manuscript.

Appendix A. Supplementary data

Supplementary data to this article can be found online at https://doi.org/10.1016/j.pocean.2023.103131.

References

Arrigo, K.R., van Dijken, G.L., 2015. Continued increases in Arctic Ocean primary production. Progress in Oceanography 136, 60–70. https://doi.org/10.1016/j.pocean.2015.05.002.

Årthun, M., Eldevik, T., Smedsrud, L.H., Skagseth, Ø., Ingvaldsen, R.B., 2012. Quantifying the influence of Atlantic heat on Barents Sea ice variability and retreat. Journal of Climate 25 (13), 4736–4743. https://doi.org/10.1175/JCLI-D-11-00466.1.

Assmy, P., Fernández-Méndez, M., Duarte, P., Meyer, A., Randelhoff, A., Mundy, C.J., Olsen, L.M., Kauko, H.M., Bailey, A., Chierici, M., Cohen, L., Doulgeris, A.P., Ehn, J. K., Fransson, A., Gerland, S., Hop, H., Hudson, S.R., Hughes, N., Itkin, P., Johnsen, G., King, J.A., Koch, B.P., Koenig, Z., Kwasniewski, S., Laney, S.R., Nicolaus, M., Pavlov, A.K., Polashenski, C.M., Provost, C., Rösel, A., Sandbu, M., Spreen, G., Smedsrud, L.H., Sundfjord, A., Taskjelle, T., Tatarek, A., Wiktor, J., Wagner, P.M., Wold, A., Steen, H., Granskog, M.A., 2017. Leads in Arctic pack ice enable early phytoplankton blooms below snow-covered sea ice. Scientific Reports 7, 40850. https://doi.org/10.1038/srep40850.

Beszczynska-Möller, A., Fahrbach, E., Schauer, U., Hansen, E., 2012. Variability in atlantic water temperature and transport at the entrance to the arctic ocean, 1997–2010. ICES Journal of Marine Science 69 (5), 852–863. https://doi.org/10.1093/icesjms/fss056.

Anglada-Ortiz, G., Meilland, J., Ziveri, P., Chierici, M., Fransson, A., Jones, E., Rasmussen, T.L., 2023. Seasonality of marine calcifiers in the northern Barents Sea: Spatiotemporal distribution of planktonic foraminifers and shelled pteropods and their contribution to carbon dynamics. Prog. Oceanogr. 218, 103121 https://doi.org/10.1016/j.pocean.2023.103121.

Bodur, Y.V., Renaud, P.E., Goraguer, L., Amargant-Arumí, M., Assmy, P., Maria Dąbrowska, A., Marquardt, M., Renner, A.H.H., Tatarek, A., Reigstad, M., 2023. Seasonal patterns of vertical flux in the northwestern Barents Sea under Atlantic Water influence and sea-ice decline. Prog. Oceanogr. 219, 103132 https://doi.org/10.1016/j.pocean.2023.103132.

Brewer, P.G., Goldman, J.C., 1976. Alkalinity changes generated by phytoplankton growth. Limnol. Ocean. 21, 108–117. https://doi.org/10.4319/lo.1976.21.1.0108.

Carmack, E., Barber, D., Christensen, J., Macdonald, R., Rudels, B., Sakshaug, E., 2006. Climate variability and physical forcing of the food webs and the carbon budget on panarctic shelves. Progress in Oceanography 71, 145–181. https://doi.org/10.1016/j.pocean.2006.10.005.

Chierici, M., Jones, E., Lødemel, H. H. 2021a. Water column data on dissolved inorganic nutrients (nitrite, nitrate, phosphate and silicic acid) from the Nansen LEGACY seasonal cruise Q3, 2019706 with R.V. Kronprins Haakon, 5-27 August 2019. https://doi.org/https://doi.org/10.21335/NMDC-1472517325.

Chierici, M., Jones, E., Lødemel, H. H. 2021b. Water column data on dissolved inorganic nutrients (nitrite, nitrate, phosphate and silicic acid) from the Nansen LEGACY seasonal cruise Q4, 2019711 with R.V. Kronprins Haakon, November - December 2019. https://doi.org/https://doi.org/10.21335/NMDC-1629206101.

Chierici, M., Fransson, A., Anderson, L.G., 1999. Influence of m-cresol purple indicator additions on the pH of seawater samples: correction factors evaluated from a chemical speciation model. Marine Chemistry 65, 281–290. https://doi.org/10.1016/S0304-4203(99)00020-1.

Chierici, M., Fransson, A., 2009. CaCO3 saturation in the surface water of the Arctic Ocean: undersaturation in freshwater influenced shelves. Biogeosciences 6, 2421–2432.

Chierici, M., Fransson, A., Lansard, B., Miller, L.A., Mucci, A., Shadwick, E., Thomas, H., Tremblay, J.E., Papakyriakou, T.N., 2011. Impact of biogeochemical processes and environmental factors on the calcium carbonate saturation state in the Circumpolar Flaw Lead in the Amundsen Gulf, Arctic Ocean. Journal of Geophysical Research 116 (C9), C00G09. https://doi.org/10.1029/2011JC007184.

Chierici, M., Vernet, M., Fransson, A., Børsheim, K.Y., 2019. Net Community Production and Carbon Exchange From Winter to Summer in the Atlantic Water Inflow to the Arctic Ocean. Frontiers in Marine Science 6. https://doi.org/10.3389/fmars.2019.00528.

Clayton, T.D., Byrne, R.H., 1993. Spectrophotometric seawater pH measurements: total hydrogen ion concentration scale calibration of m-cresol purple and at-sea results. Deep-Sea Research 1, 40(10), 2115–2129.

Cooper, L.W., McClelland, J.W., Holmes, R.M., Raymond, P.A., Gibson, J.J., Guay, C.K., Peterson, B.J., 2008. Flow-weighted values of runoff tracers d18O, DOC, Ba, alkalinity from the six largest Arctic rivers. Geophysical Research Letters 35, L18606. https://doi.org/10.1029/2008GL035007.

Dickson, A.G., 1990. Standard potential of the reaction: AgCl(s) + 1/2H2 (g) = Ag(s) + HCl(aq), and the standard acidity constant of the ion HSO4- in synthetic sea water from 273.15 to 318.15 K. Journal of Chemical Thermodynamics 22, 113–127. https://doi.org/10.1016/0021-9614(90)90074-Z.

Dickson, A.G., Millero, F.J., 1987. A comparison of the equilibrium constants for the dissociation of carbonic acid in seawater media. Deep-Sea Research Part A 34, 1733–1743. https://doi.org/10.1016/0198-0149(87)90021-5.

Dickson, A.G., Sabine, C.L., Christian, J.R. (Eds.), 2007. Guide to Best Practices for Ocean CO2 Measurements. PICES Special Publication 3. IOCCP Report 8. North Pacific Marine Science Organization, Sidney, Canada.

Dieckmann, G., Nehrke, G., Uhlig, C., Göttlicher, J., Gerland, S., Granskog, M.A., Thomas, D.N., 2010. Ikaite CaCO3. 6H2O discovered in Arctic sea ice. The Cryosphere 4, 227–230.

Doney, S.C., Balch, W.M., Fabry, V.J., Feely, R.A., 2009. Ocean acidification: A critical emergingproblem for the ocean sciences. Oceanography 224, 16–25. https://www.jstor.org/stable/24861020.

Duarte, P., Sundfjord, A., Meyer, A., Hudson, S. R., Spreen, G., Smedsrud, L. H. 2020. Warm Atlantic water explains observed sea ice melt rates north of Svalbard. Journal of Geophysical Research: Oceans, 125, e2019JC015662. https://doi.org/10.1029/2019JC015662.

Ericson, Y., Chierici, M., Falck, E., Fransson, A., Jones, E.M., Kristiansen, S., 2019. Seasonal dynamics of the marine CO2 system in Adventfjorden, a West Spitsbergen fjord. Polar Research 38, 3345. https://doi.org/10.33265/polar.v38.3345.

Ericson, Y., Fransson, A., Chierici, M., Jones, E.M., Skjelvan, I., Omar, A., Olsen, A., Becker, M., 2023. Rapid fCO2 rise in the northern Barents Sea and Nansen Basin. Prog. Oceanogr. 217, 103079 https://doi.org/10.1016/j.pocean.2023.103079.

Ericson, Y., Ulfsbo, A., van Heuven, S., Kattner, G., Anderson, L.G., 2014. Increasing carbon inventory of the intermediate layers of the Arctic Ocean. Journal of Geophysical Research, Oceans 1194, 2312–2326. https://doi.org/10.1002/2013JC009514.

Fransson, A., Chierici, M., Anderson, L.G., Bussman, I., Jones, E.P., Swift, J.H., 2001. The importance of shelf processes for the modification of chemical constituents in the waters of the eastern Arctic Ocean: implication for carbon fluxes. Continental Shelf Research 21, 225–242. https://doi.org/10.1016/s0278-4343(00)00088-1.

Fransson, A., Chierici, M., Miller, L.A., Carnat, G., Shadwick, E., Thomas, H., Pineault, S., Papakyriakou, T.N., 2013. Impact of sea-ice processes on the carbonate system and ocean acidification at the ice-water interface in the Arctic Ocean. Journal of Geophysical Research, Oceans 118, 1–23. https://doi.org/10.1002/2013JC009164.

Fransson, A., Chierici, M., Skjelvan, I., Olsen, A., Assmy, P., Peterson, A., Spreen, G., Ward, B., 2017. Effect of sea-ice and biogeochemical processes and storms on under-ice water fCO2 during the winter-spring transition in the high Arctic Ocean: implications for sea-air CO2 fluxes. Journal of Geophysical Research, Oceans 122, 5566–5587. https://doi.org/10.1002/2016JC012478.

Frigstad, H., Andersen, T., Bellerby, R.G.J., Silyakova, A., Hessen, D.O., 2014. Variation in the seston C: N ratio of the Arctic Ocean and pan-Arctic shelves. J. Mar. Sys. 129, 214–223. https://doi.org/10.1016/j.jmarsys.2013.06.004.

Friis, K., Körtzinger, A., Wallace, D.W.R., 2003. The salinity normalization of marine inorganic carbon chemistry data. Geophysical Research Letters 30, 1085. https://doi.org/10.1029/2002GL015898.

Gerland, S. 2022. CTD data from Nansen Legacy Cruise - Seasonal Cruise Q1. [Data set] https://doi.org/10.21335/NMDC-1491279668.

Grasshoff, K., Kremling, K., Ehrhardt, M., 2009. Methods of seawater analysis, 3rd ed. John Wiley, New York.

Gundersen, K., Møgster, J.S., Lien, V.S., Ershova, E., Lunde, L.F., Arnesen, H., Olsen, A.K., 2022. Thirty years of nutrient biogeochemistry in the Barents Sea and the adjoining Arctic Ocean, 1990–2019. Scientific Data 9, 649. https://doi.org/10.1038/s41597-022-01781-w.

Hegseth, E.N., Sundfjord, A., 2008. Intrusion and blooming of Atlantic phytoplankton species in the high Arctic. Journal of Marine Systems 74, 108–119. https://doi.org/10.1016/j.jmarsys.2007.11.011.

Henley, S.F., Porter, M., Hobbs, L., Braun, J., Cuillaume-Castel, R., Venables, E.J., Dumont, E., Cottier, F., 2020. Nitrate supply and uptake in the Atlantic Arctic sea ice zone: seasonal cycle, mechanisms and drivers. Philosophical Transactions of the Royal Society A 378, 20190361. https://doi.org/10.1098/rsta.2019.0361.

Ingvaldsen, R.B., Assmann, K.M., Primicerio, R., Fossheim, M., Polyakov, I.V., Dolgov, A. V., 2021. Physical manifestations and ecological implications of Arctic Atlantification. Nature Reviews Earth Environment 2 (12), 874–889. https://doi.org/10.1038/s43017-021-00228-x.

Jakobsson, M., Mayer, L., Coakley, B., Dowdeswell, J.A., Forbes, S., Fridman, B., Hodnesdal, H., Noormets, R., Pedersen, R., Rebesco, M., Schenke, H.W., Zarayskaya, Y., Accettella, D., Armstrong, A., Anderson, R.M., Bienhoff, P., Camerlenghi, A., Church, I., Edwards, M., Gardner, J.V., Hall, J.K., Hell, B., Hestvik, O., Kristoffersen, Y., Marcussen, C., Mohammad, R., Mosher, D., Nghiem, S. V., Pedrosa, M.T., Travaglini, P.G., Weatherall, P., 2012. The International Bathymetric Chart of the Arctic Ocean IBCAO Version 3.0. Geophysical Research Letters 39, 1–6. https://doi.org/10.1029/2012GL052219.

Johnson, K.M., Sieburth, J.M., Williams, P.J.L., Brändström, L., 1987. Coulometric total carbon dioxide analysis for marine studies - automation and calibration. Marine Chemistry 21, 117–133. https://doi.org/10.1016/0304-42038790033-8.

Jones EM, Chierici M, Skjelvan I, Norli M, Børsheim KY, Lødemel HH, Sørensen K, King AL, Lauvset S, Jackson K, de Lange T, Johannessen T, Mourgues C. 2019. Monitoring ocean acidification in Norwegian seas in 2018. Rapport, Miljødirektoratet. M-1417.

Jones, E.M., Chierici, M., Menze, S., Fransson, A., Ingvaldsen, R.B., Lødemel, H.H., 2021. Ocean acidification state variability of the Atlantic Arctic Ocean around northern Svalbard. Prog. Ocean. 199, 102708. https://doi.org/10.1016/j.pocean.2021.102708.

Jones, E.M., Chierici, M., Skjelvan, I., Norli, M., Frigstad, H., Børsheim, K.Y., Lødemel, H. H., Kutti, T., King, A.L., Sørensen, K., Lauvset, S.K., Jackson-Misje, K., Apelthun, L.B., de Lange, T., Johannessen, T., Mourgues, C., Bellerby, R., 2020. Monitoring ocean acidification in Norwegian seas in 2019. Rapport Miljødirektoratet M-1735.

Jones E., Chierici M., Lødemel H.H., Møgster J., Fonnes L. 2022a. Water column data on dissolved inorganic nutrients (nitrite, nitrate, phosphate and silicic acid) from Process (P) stations during the Nansen LEGACY seasonal cruise Q1, 2021703, with R. V. Kronprins Haakon, 4-17 March 2021. https://doi.org/10.21335/NMDC-762320451.

Jones E., Chierici M., Lødemel H.H., Møgster J., Fonnes L. 2022b. Water column data on dissolved inorganic nutrients (nitrite, nitrate, phosphate and silicic acid) from Process (P) stations during the Nansen LEGACY seasonal cruise Q2, 2021704, with R. V. Kronprins Haakon, 30 April - 18 May 2021. https://doi.org/10.21335/NMDC-487023368.

Jones EM, Skjelvan I, Frigstad H, Chierici M, Lødemel HH, Kutti T, King AL, Omar A, Christensen G, Marty S, Protsenko E, Mengeot C, Valestrand L, Jacard, PF, Jackson-Misje K, de Lange T, Becker, M, Mourgues C. 2022c. Monitoring ocean acidification in Norwegian seas in 2021 – selected results. Rapport Miljødirektoratet. M-2311.

Koenig, Z, Fer, I., Chierici. M, Fransson, A., Jones, E. Kolas, E.H. this issue, a. Diffusive and advective fluxes of inorganic nutrients and dissolved inorganic carbon in the Barents Sea in autumn.

Koenig, Z, Lind, S, Lundesgaard, Ø, Muilwijk, M, Sandven, H, Assmy, P, Assmann, K, Chierici, M, Fransson, A, Gerland, S, Jones, E, Renner, AHH, Granskog, MA. this issue, b. Winter to Late Summer in the Northwestern Barents Sea Shelf: Sea Ice and Upper Ocean Evolution and Impacts on Nutrient and Phytoplankton Dynamics.

Lee, K., Kim, T.-W., Byrne, R.H., Millero, F.J., Feely, R.A., Liu, Y.-M., 2010. The universal ratio of boron to chlorinity for the North Pacific and North Atlantic oceans. Geochimica Et Cosmochimica Acta 74, 1801–1811. https://doi.org/10.1016/j.gca.2009.12.027.

Nansen Legacy. 2022. Sampling Protocols: Version 10. The Nansen Legacy Report Series 32/2022. https://doi.org/10.7557/nlrs.6684.

Leu, E., Søreide, J.E., Hessen, D.O., Falk-Petersen, S., Berge, J., 2011. Consequences of changing sea-ice cover for primary and secondary producers in the European Arctic shelf seas: timing, quantity, and quality. Progress in Oceanography 90, 18–32. https://doi.org/10.1016/j.pocean.2011.02.004.

Lind, S., Ingvaldsen, R.B., Furevik, T., 2018. Arctic warming hotspot in the northern Barents Sea linked to declining sea-ice import. Nature Climate Change 8 (7), 634–639. https://doi.org/10.1038/s41558-018-0205-y.

Loeng, H., 1991. Features of the physical oceanographic conditions in the Barents Sea. Polar Research 10 (1), 5–18. https://doi.org/10.3402/polar.v10i1.6723.

Ludvigsen, M. 2022. CTD data from Nansen Legacy Cruise - Seasonal cruise Q2. [Data set] https://doi.org/10.21335/NMDC-515075317.

Lundesgaard, Ø., Sundfjord, A., Renner, A. H. 2021. Drivers of interannual sea ice concentration variability in the Atlantic water inflow region north of Svalbard. Journal of Geophysical Research: Oceans, 126(4), e2020JC016522. https://doi.org/10.1029/2020JC016522.

Lundesgaard, Ø., Sundfjord, A., Lind, S., Nilsen, F., Renner, A.H., 2022. Import of Atlantic Water and sea ice controls the ocean environment in the northern Barents Sea. Ocean Science 18 (5), 1389–1418. https://doi.org/10.5194/os-18-1389-2022.

Mehrbach, C., Culberson, C.H., Hawley, J.E., Pytkowicz, R.M., 1973. Measurement of the apparent dissociation constants of carbonic acid in seawater at atmospheric pressure. Limnology and Oceanography 18, 897–907. https://doi.org/10.4319/lo.1973.18.6.0897.

Millero, F.J., 1979. The thermodynamics of the carbonate system in seawater. Geochimica Et Cosmochimica Acta 43, 1651–1661. https://doi.org/10.1016/0016-7037(79)90184-4.

Mucci, A., 1983. The solubility of calcite and aragonite in seawater at various salinities, temperatures, and one atmosphere total pressure. American Journal of Science 283, 780–799. https://doi.org/10.2475/ajs.283.7.780.

Neukermans, G., Oziel, L., Babin, M., 2018. Increased intrusion of warming Atlantic water leads to rapid expansion of temperate phytoplankton in the Arctic. Global Change Biology 24, 2545–2553. https://doi.org/10.1111/gcb.14075.

Onarheim, I.H., Smedsrud, L.H., Ingvaldsen, R.B., Nilsen, F., 2014. Loss of sea ice during winter north of Svalbard. Tellus a: Dynamic Meteorology and Oceanography 66 (1), 23933. https://doi.org/10.3402/tellusa.v66.23933.

Orr, J.C., Fabry, V.J., Aumont, O., Bopp, L., Doney, S.C., Feely, R.A., Gnanadesikan, A., Gruber, N., Ishida, A., Joos, F., 2005. Anthropogenic ocean acidification over the twenty-first century and its impact on calcifying organisms. Nature 437 (7059), 681–686.

Oziel, L., Sirven, J., Gascard, J.-C., 2016. The Barents Sea frontal zones and water masses variability (1980–2011). Ocean Science 12, 169–184. https://doi.org/10.5194/os-12-169-2016.

Oziel, L., Baudena, A., Ardyna, M., Massicotte, P., Randelhoff, A., Sallée, J.B., Ingvaldsen, B., Devred, E., Babin, M., 2020. Faster Atlantic currents drive poleward expansion of temperate phytoplankton in the Arctic Ocean. Nature Communications 11, 1705. https://doi.org/10.1038/s41467-020-15485-5.

Pierrot, D., Lewis, E., Wallace, D.W.R., 2006. MSExcel Program developed for CO2 system calculations, ORNL/CDIAC-105. Carbon Dioxide Information Analysis Center, Oak Ridge National Laboratory, US Department of Energy, Oak Ridge, Tennessee.

Polyakov, I.V., Pnyushkov, A.V., Alkire, M.B., Ashik, I.M., Baumann, T.M., Carmack, E. C., Yulin, A., 2017. Greater role for Atlantic inflows on sea-ice loss in the Eurasian Basin of the Arctic Ocean. Science 356 (6335), 285–291. https://doi.org/10.1126/science.aai8204.

Randelhoff, A., Reigstad, M., Chierici, M., Sundfjord, A., Ivanov, V., Cape, M.R., Vernet, M., Tremblay, J.-E., Bratbak, G., Kristiansen, S. 2018. Seasonality of the physical and biogeochemical hydrography in the inflow to the Arctic Ocean through Fram Strait. Front. Mar. Sci. 5, 1–16. doi:10.3389/ fmars.2018.00224.

Randelhoff, A., Sundfjord, A., Reigstad, M., 2015. Seasonal variability and fluxes of nitrate in the surface waters over the Arctic shelf slope. Geophysical Research Letters 3442–3449. https://doi.org/10.1002/2015GL063655.

Randelhoff, A., Sundfjord, A., 2018. Short commentary on marine productivity at Arctic shelf breaks: upwelling, advection and vertical mixing. Ocean Science 14, 293–300. https://doi.org/10.5194/os-14-293-2018.

Redfield, A., Ketchum, B. H., and Richards, F. A. 1963. "The influence of organisms on the composition of sea water," in The Sea, Vol. 2, ed. M. N. Hill (New York, NY: Interscience), 26–77.

Reigstad, M., Wassmann, P., Riser, C.W., Øygarden, S., Rey, F., 2002. Variations in hydrography, nutrients and chlorophyll a in the marginal ice-zone and the central Barents Sea. Journal of Marine Systems 38 (1–2), 9–29. https://doi.org/10.1016/S0924-7963(02)00167-7.

Reigstad, M. (2022). CTD data from Nansen Legacy Cruise - Seasonal cruise Q3. [Data set] https://doi.org/https://doi.org/10.21335/NMDC-1107597377.

Renner, A.H.H., Sundfjord, A., Janout, M.A., Ingvaldsen, R.B., Beszczynska-Möller, A., Pickart, R.S., Pérez-Hernández, M.D., 2018. Variability and redistribution of heat in the Atlantic Water boundary current north of Svalbard. Journal of Geophysical Research: Oceans 123 (9), 6373–6391. https://doi.org/10.1029/2018JC013814.

Riley, J.P., Tongudai, M., 1967. The major cation/chlorinity ratios in sea water. Chemical Geology 2, 263–269.

Rogge, A., Janout, M., Loginova, N., Trudnowska, E., Hörstmann, C., Wekerle, C., Oziel, L., Schourup-Kristensen, V., Ruiz-Castillo, E., Schulz, K., Povazhnyy, V.V., 2023. Carbon dioxide sink in the Arctic Ocean from cross-shelf transport of dense Barents Sea water. Nature Geoscience 16 (1), 82–88. https://doi.org/10.1038/s41561-022-01069-z.

Rysgaard, S., Glud, R.N., Sejr, M.K., Bendtsen, J., Christensen, P.B., 2007. Inorganic carbon transport during sea ice growth and decay: a carbon pump in polar seas. Journal of Geophysical Research 112, C03016. https://doi.org/10.1029/2006JC003572.

Renner, AHH, Bailey, A, Reigstad, M., Sundfjord, A., Chierici, M., Jones, EM. (this issue). Late summer hydrography, inorganic nutrients and chlorophyll a linked to sea ice cover in the Atlantic Water inflow region north of Svalbard.

Schlitzer, R., 2022. Ocean Data View. http://www.odw.awi.de.

Skagseth, Ø., Eldevik, T., Årthun, M., Asbjørnsen, H., Lien, V.S., Smedsrud, L.H., 2020. Reduced efficiency of the Barents Sea cooling machine. Nature Climate Change. 10 (7), 661–666.

Skjelvan I, Jones EM, Chierici M, Frigstad H, Børsheim KY, Lødemel HH, Kutti T, King AL, Sørensen K, Omar A, Bellerby R, Christensen G, Marty S, Protsenko E, Mengeot C, Valestrand L, Norli M, Jackson-Misje K, Apelthun LB, de Lange T, Johannessen T, Mourgues C. 2021. Monitoring ocean acidification in Norwegian seas in 2020, Rapport, Miljødirektoratet, M-2056.

Slagstad, D., Wassmann, P.F.J., Ellingsen, I., 2015. Physical constrains and productivity in the future Arctic Ocean. Frontiers in Marine Science 2, 1–23. https://doi.org/10.3389/fmars.2015.00085.

Smedsrud, L.H., Esau, I., Ingvaldsen, R.B., Eldevik, T., Haugan, P.M., Li, C., Sorokina, S. A., 2013. The role of the Barents Sea in the Arctic climate system. Reviews of Geophysics 51 (3), 415–449. https://doi.org/10.1002/rog.20017.

Smedsrud, L. H., Muilwijk, M., Brakstad, A., Madonna, E., Lauvset, S. K., Spensberger, C., ... Årthun, M. (2022). Nordic Seas heat loss, Atlantic inflow, and Arctic sea ice cover over the last century. Reviews of Geophysics, 60(1), e2020RG000725. https://doi.org/10.1029/2020RG000725.

Søreide, J. E. (2022). CTD data from Nansen Legacy Cruise - Seasonal cruise Q4. [Data set] https://doi.org/https://doi.org/10.21335/NMDC-301551919.

Spreen, G., Kaleschke, L., Heygster, G., 2008. Sea ice remote sensing using AMSR-E 89 GHz channels. Journal of Geophysical Research 113, C02S03. https://doi.org/10.1029/2005JC003384.

Sundfjord, A., Assmann, K. M., Lundesgaard, Ø., Renner, A. H., Lind, S., Ingvaldsen, R. B. 2020. Suggested water mass definitions for the central and northern Barents Sea, and the adjacent Nansen Basin: Workshop Report. The Nansen Legacy Report Series, (8). https://doi.org/10.7557/nlrs.5707.

Tremblay, J.E., Anderson, L.G., Matrai, P., Coupel, P., Bélanger, S., Michel, C., Reigstad, M., 2015. Global and regional drivers of nutrient supply, primary production and CO2 drawdown in the changing Arctic Ocean. Prog. Ocean. 139, 171–196. https://doi.org/10.1016/j.pocean.2015.08.009.

Ulfsbo, A., Jones, E.M., Casacuberta, N., Korhonen, M., Rabe, B., Karcher, M., van Heuven, S.M.A.C., 2018. Rapid changes in anthropogenic carbon storage and ocean acidification in the intermediate layers of the Eurasian Arctic Ocean, 1996–2015. Glob. Biogeochem. Cycles 32, 1254–1275. https://doi.org/10.1029/2017GB005738.

Van Engeland, T., Bagøien, E., Wold, A., Cannaby, H.A., Majaneva, S., Vader, A., Rønning, J., Handegard, N.O., Dalpadado, P., Ingvaldsen, R.B., 2023. Diversity and seasonal development of large zooplankton along physical gradients in the Arctic Barents Sea. Prog. Ocean. 103065 https://doi.org/10.1016/j.pocean.2023.103065.

Wassmann, P.F., Reigstad, M., Haug, T., Rudels, B., Carroll, M., Hop, H., Wing-Gabrielsen, G., Falk-Petersen, S., Denisenko, S.G., Arashkevich, E., Slagstad, D., Pavlova, O., 2006. Food webs and carbon flux in the Barents Sea. In Structure and function of contemporary food webs on Arctic shelves: a panarctic comparison. Prog. Ocean. 71, 2–4. https://doi.org/10.1016/j.pocean.2006.10.0.

Yamamoto-Kawai, M., McLaughlin, F.A., Carmack, E.C.S., Nishino, S., Shimada, K., 2009. Aragonite undersaturation in the Arctic Ocean: Effects of ocean acidification and sea ice melt. Science 326, 1098–1100. https://doi.org/10.1126/science.1174190.

Zamelczyk, K., Fransson, A., Chierici, M., Jones, E., Meilland, J., Anglada-Ortiz, G., Hodal Lødemel, H., 2021. Distribution and abundances of planktic foraminifera and

shelled pteropods during the polar night in the sea-ice covered northern Barents Sea. Front. Mar. Sci. 1516 https://doi.org/10.3389/fmars.2021.644094.
Zeebe, R., Wolf-Gladrow, D., 2001. CO2 in Seawater: Equilibrium, Kinetics, Isotopes. Elsevier Science, Amsterdam.
Zhang, Y., Yamamoto-Kawai, M., Williams, W.J., 2020. Two decades of ocean acidification in the surface waters of the Beaufort Gyre, Arctic Ocean: Effects of sea ice melt and retreat from 1997–2016. Geophys. Res. Lett. 47, e60119. https://doi.org/10.1029/2019GL086421.